

# Supersonic and Hypersonic Flows on 2D Unstructured Context: Part V The Last Model – Final Conclusions

Edisson S. G. Maciel

**Abstract**—In this work, the fifth of this study, numerical simulations involving supersonic and hypersonic flows on an unstructured context are analyzed. The Steger and Warming, the Van Leer, the Liou and Steffen Jr., and the Radespiel and Kroll schemes are implemented on a finite volume formulation, using unstructured spatial discretization. The algorithms are implemented in their first order spatial accuracy. To the turbulent simulations, the Van Leer and the Radespiel and Kroll algorithms are implemented with the Rumsey et al. model. The air inlet problem to the hypersonic inviscid simulations, and the re-entry capsule problem to the hypersonic viscous simulations are studied. The results have demonstrated that the Van Leer algorithm yields the best results in terms of the prediction of the shock angle of the oblique shock waves in the air inlet problem and the best value of the stagnation pressure at the configuration nose in the re-entry capsule configuration. The spatially variable time step is the best choice to accelerate the convergence of the numerical schemes, as reported by Maciel. In terms of turbulent results, the Rumsey et al. model yields good results, proving the good capacity of this turbulence model in simulate hypersonic flows. This paper is the conclusion of Maciel's works started in 2011 and treats mainly the influence of the turbulence model on the solution quality.

**Keywords**—Unstructured spatial discretization; Euler and Navier-Stokes equations; Steger and Warming algorithm; Van Leer algorithm; Liou and Steffen Jr. algorithm; Radespiel and Kroll algorithm; Rumsey et al. turbulence model.

## I. INTRODUCTION

CONVENTIONAL non-upwind algorithms have been used extensively to solve a wide variety of problems ([1]). Conventional algorithms are somewhat unreliable in the sense that for every different problem (and sometimes, every different case in the same class of problems) artificial dissipation terms must be specially tuned and judiciously chosen for convergence. Also, complex problems with shocks and steep compression and expansion gradients may defy solution altogether.

Upwind schemes are in general more robust but are also more involved in their derivation and application. Some upwind schemes that have been applied to the Euler equations

are, for example, [2-4, 6]. Some comments about these methods are reported below:

[2] developed a method that used the remarkable property that the nonlinear flux vectors of the inviscid gasdynamic equations in conservation law form were homogeneous functions of degree one of the vector of conserved variables. This property readily permitted the splitting of the flux vectors into subvectors by similarity transformations so that each subvector had associated with it a specified eigenvalue spectrum. As a consequence of flux vector splitting, new explicit and implicit dissipative finite-difference schemes were developed for first-order hyperbolic systems of equations.

[3] suggested an upwind scheme based on the flux vector splitting concept. This scheme considered the fact that the convective flux vector components could be written as flow Mach number polynomial functions, as main characteristic. Such polynomials presented the particularity of having the minor possible degree and the scheme had to satisfy seven basic properties to form such polynomials. This scheme was presented to the Euler equations in Cartesian coordinates and three-dimensions.

[4] proposed a new flux vector splitting scheme. They declared that their scheme was simple and its accuracy was equivalent and, in some cases, better than the [5] scheme accuracy in the solutions of the Euler and the Navier-Stokes equations. The scheme was robust and converged solutions were obtained so fast as the [5] scheme. The authors proposed the approximated definition of an advection Mach number at the cell face, using its neighbor cell values via associated characteristic velocities. This interface Mach number was so used to determine the upwind extrapolation of the convective quantities.

[6] emphasized that the [4] scheme had its merits of low computational complexity and low numerical diffusion as compared to other methods. They also mentioned that the original method had several deficiencies. The method yielded local pressure oscillations in the shock wave proximities, adverse mesh and flow alignment problems. In the [6] work, a hybrid flux vector splitting scheme, which alternated between the [4] scheme and the [3] scheme, in the shock wave regions, was proposed, assuring that resolution of strength shocks was clear and sharply defined.

Algorithms for solving the Euler equations using a perfect

Edisson S. G. Maciel works as a post-doctorate researcher at ITA (Aeronautical Technological Institute), Aeronautical Engineering Division – Praça Marechal do Ar Eduardo Gomes, 50 – Vila das Acácias – São José dos Campos – SP – Brazil – 12228-900 (corresponding author, phone number: +55 012 99165-3565; e-mail: [edisavio@edissavio.eng.br](mailto:edisavio@edissavio.eng.br)).

gas model on structured grids in two- and three-dimensions have become widespread in recent years ([7-8]). However, these algorithms have shown difficulties in predicting satisfactory results around complex geometries due to mesh irregularities. As a result, attention has turned to the development of solution algorithms on arbitrary unstructured grids. Impressive results have been obtained for a wide range of problems ([9-10]).

One problem associated with unstructured meshes is the increased difficulty in obtaining smooth higher order spatial approximations to state data at cell interfaces. Two methods have been used to obtain higher order accuracy on unstructured meshes. A method used by several researchers for cell vertex schemes ([11-12]) was applied to obtain higher order accuracy in a procedure analogous to MUSCL differencing on a structured mesh. A conventional structured mesh limiter can be employed in this scheme to obtain approximately monotone results near flow discontinuities. The second method, which was proposed by [10], linearly reconstructs the cell averaged data and imposes a monotone preserving limiter to achieve smooth results near flow discontinuities.

On an unstructured algorithm context, [13-14] has presented a work involving the numerical implementation of four typical algorithms of the Computational Fluid Dynamics community. The [2-3, 5, 15] algorithms were implemented and applied to the solution of aeronautical and of aerospace problems, in two-dimensions. The Euler equations in conservative form, employing a finite volume formulation and an unstructured spatial discretization, were solved. The [5] and the [15] schemes were flux difference splitting ones and more accurate solutions were expected. On the other hand, the [2-3] schemes were flux vector splitting ones and more robustness properties were expected. The time integration was performed by a Runge-Kutta method of five stages. All four schemes were first order accurate in space and second order accurate in time. The steady state physical problems of the transonic flow along a convergent-divergent nozzle and of the supersonic flows along a ramp and around a blunt body were studied. The results have shown that the [5] scheme has presented the most severe pressure fields in the ramp and blunt body problems and the most accurate value of the stagnation pressure in the blunt body case. On the other hand, the [3] scheme has yielded the most accurate value of the shock angle in the ramp problem, while the [15] scheme has yielded the best value of the lift coefficient in the blunt body problem.

Following the studies of 2007, [16-17] has presented a work involving the numerical implementation of more three typical algorithms of the Computational Fluid Dynamics community. The [4, 6, 18] algorithms were implemented and applied to the solution of aeronautical and aerospace problems, in two-dimensions. The Euler equations in conservative form, employing a finite volume formulation and an unstructured spatial discretization, were solved. The [18] scheme was a flux difference splitting one and more accurate solutions were

expected. On the other hand, the [4, 6] schemes were flux vector splitting ones and more robustness properties were expected. The time integration was performed by a Runge-Kutta method of five stages. All three schemes were first order accurate in space and second order accurate in time. The steady state physical problems of the transonic flow along a convergent-divergent nozzle, of the supersonic flows along a ramp and around a blunt body, and of the "cold gas" hypersonic flow around a double ellipse were studied. The results have shown that the [18] scheme presents the most severe pressure fields and the most accurate values of the stagnation pressure in the blunt body and in the double ellipse problems. On the other hand, the [3] scheme yields the best wall pressure distribution, in comparison with the experimental results, in the nozzle problem, whereas the [4] scheme yields the most accurate value of the shock angle in the ramp problem.

In relation to high resolution unstructured solutions, [19-20] has presented a work involving [4, 6] schemes implemented on a finite volume context and using an upwind and unstructured spatial discretization to solve the Euler equations in the two-dimensional space. Both schemes were flux vector splitting ones. These schemes were implemented in their second order accuracy versions employing the linear reconstruction procedure of [10] and their results were compared with their first order accuracy versions and with theoretical results. Five nonlinear flux limiters were studied: Barth and Jespersen (minmod like), Van Leer, Van Albada, Super Bee and  $\beta$ -limiter. The time integration used a Runge-Kutta method of five stages and was second order accurate. Both algorithms were accelerated to the steady state solution using a spatially variable time step procedure. This technique has proved excellent gains in terms of convergence ratio as reported in [21-22]. The algorithms were applied to the solution of the steady state physical problem of the supersonic flow along a compression corner. The results have shown that the [6] scheme using Barth and Jespersen, Van Leer, Van Albada and Super Bee nonlinear limiters presented the most accurate values to the shock angle of the oblique shock wave generated at the compression corner.

In 2010, [23-24] has implemented the [3] and [5] algorithms, on a finite volume context and employing an upwind and unstructured spatial discretization, to solve the Euler equations in two-dimensions. The [5] scheme was a flux difference splitting type algorithm, whereas the [3] scheme was a flux vector splitting type algorithm. Both algorithms were implemented in their second order versions, employing the [10] linear reconstruction procedure and their results were compared with their first order version solutions and theoretical results. Five non-linear flux limiters were studied: Barth and Jespersen (minmod), Van Leer, Van Albada, Super Bee and  $\beta$ -limiter. The Runge-Kutta method of five stages, second order accurate, was used to perform time integration. The steady state physical problem of the supersonic flow along a compression corner was studied. A spatially variable time

step procedure was employed to accelerate the convergence of the numerical schemes to the steady state solution. Effective gains in terms of convergence acceleration were reported in [21-22]. The results have demonstrated that the [5] scheme in its second order version, using the Van Albada and Super Bee limiters, yielded the most accurate solutions.

In terms of turbulence studies, [25-26] has developed interesting investigation involving the turbulence models of [27-28] applied to the steady state problem of the supersonic flow along a ramp. The [29-30] algorithms were implemented and used to perform the numerical experiments. Both schemes were second order accurate in space and time. The [29] algorithm was a Lax-Wendroff type one and the time integration was performed in conjunction with the spatial discretization. The time integration was of predictor/corrector type. The [30] scheme was a symmetrical one and the time integration was performed according to a Runge-Kutta method. The Favre-averaged Navier-Stokes equations were solved, according to a finite volume formulation and on a structured spatial discretization context, and the [27-28] models were employed to describe the turbulence effects in the mean flow properties. A spatially variable time step procedure was employed to accelerate the convergence of [29-30] in the experiments. The results have demonstrated that the [30] algorithm predicts a pressure field more severe than that obtained by the [29] one, as the turbulent flow is studied, a more real situation, to both models. The pressure distribution along the ramp obtained by the [29-30] schemes presented the expected behavior in the turbulent solution generated by the [27] model, whereas the laminar solution simulated a weaker shock wave ahead of the ramp. In the case with the [28] model, only the solution obtained with the [30] scheme presented the expected pressure distribution behavior. In general terms, the [30] algorithm has presented the best solutions.

[31] has presented a work where the [3] flux vector splitting scheme was implemented, on a finite-volume context. The two-dimensional Favre-averaged Navier-Stokes equations were solved using an upwind discretization on a structured mesh. The [32-33] two-equation turbulence models were used in order to close the problem. The physical problems under studies were the low supersonic flow along a ramp and the moderate supersonic flow around a blunt body configuration. The implemented scheme used a MUSCL (Monotone Upstream-centered Schemes for Conservation Laws) procedure to reach second order accuracy in space. The time integration used a Runge-Kutta method of five stages and was second order accurate. The algorithm was accelerated to the steady state solution using a spatially variable time step. This technique has proved excellent gains in terms of convergence rate as reported in [21-22]. The results have demonstrated that the [33] model has yielded more critical pressure fields than the ones due to [32]. The shock angle of the oblique shock wave in the ramp problem and the stagnation pressure ahead of the blunt body configuration are better predicted by the [33] turbulence model.

[34-35] analyzed numerical simulations involving supersonic and hypersonic flows on an unstructured context. Based on the experiences performed in the structured and unstructured contexts aforementioned, the [3, 6] algorithms were implemented on a finite volume formulation, using unstructured spatial discretization. The algorithms were implemented in their first and second order spatial accuracies. The second order spatial accuracy was obtained by a linear reconstruction procedure based on the work of [10]. Several non-linear limiters were studied, as well two types of linear interpolation, based on the works of [18; 36]. Two types of viscous calculation to the laminar case were compared. They were programmed considering the works of [36-37]. To the turbulent simulations, the  $k-\omega_2$  two-equation model of [33] was employed, considering the good experience observed by the present author in the structured case. The ramp problem to the inviscid simulations and the re-entry capsule problem to the hypersonic simulations were considered. A spatially variable time step procedure was implemented aiming to obtain fast convergence rates to the two algorithms, as reported by [21-22]. Five options of time step were described and studied. The results have demonstrated that the [3] algorithm has yielded the best solution in terms of the prediction of the shock angle of the oblique shock wave in the ramp problem and the best value of the stagnation pressure at the configuration nose of the re-entry capsule problem. In terms of turbulent results, the [33] model has yielded good results, proving the good capacity of this turbulence model to high hypersonic flows.

In [38-39] the numerical simulations involving supersonic and hypersonic flows on an unstructured context are analysed, giving continuation to the [34-35] studies. The [3, 6] schemes were implemented on a finite volume formulation, using unstructured spatial discretization. The algorithms were implemented in their first and second order spatial accuracies. The second order spatial accuracy was obtained by a linear reconstruction procedure based on the work of [10]. Several non-linear limiters were studied using the linear interpolation based on the work of [36]. To the turbulent simulations, the [40-42] models were employed. The compression corner problem to the supersonic inviscid simulations and the re-entry capsule problem to the hypersonic viscous simulations were studied. The results have demonstrated that the [3] algorithm has yielded the best results in terms of the prediction of the shock angle of the oblique shock wave in the compression corner problem and the best value of the stagnation pressure at the configuration nose in the re-entry capsule configuration. The spatially variable time step is the best choice to accelerate the convergence of the numerical schemes, as reported by [21-22]. In terms of turbulent results, the [40] model has yielded the best results, proving the good capacity of this turbulence model in simulate high hypersonic flows. This paper is the conclusion of Maciel's works started in 2011 and treated mainly the influence of the turbulence model on the solution quality.

In this work, the fifth of this study, numerical simulations involving supersonic and hypersonic flows on an unstructured context are analysed. The [2-4, 6] schemes are implemented on a finite volume formulation, using unstructured spatial discretization. The algorithms are implemented in their first order spatial accuracy. To the turbulent simulations, the [43] model is employed. The air inlet problem to the hypersonic inviscid simulations and the re-entry capsule problem to the hypersonic viscous simulations are studied. The results have demonstrated that the [3] algorithm has yielded the best results in terms of the prediction of the shock angle of the oblique shock wave in the air inlet problem and the best value of the stagnation pressure at the configuration nose in the re-entry capsule configuration. The spatially variable time step is the best choice to accelerate the convergence of the numerical schemes, as reported by [21-22]. In terms of turbulent results, the [43] model yields good results, proving the good capacity of this turbulence model in simulate high hypersonic flows. This paper is the final study of Maciel's works started in 2011 and treats mainly the influence of the turbulence model on the solution quality.

II. NAVIER-STOKES EQUATIONS

The two-dimensional flow is modeled by the Navier-Stokes equations, which express the conservation of mass and energy as well as the momentum variation of a viscous, heat conducting and compressible media, in the absence of external forces. The Euler equations are obtained in the limiting case of an infinity Reynolds number or, in other words, neglecting the viscous vectors. So, their description is omitted. The integral form of the Navier-Stokes equations may be represented by:

$$\partial/\partial t \int_V QdV + \int_S [(E_e - E_v)n_x + (F_e - F_v)n_y]dS + \int_V GdV = 0, \quad (1)$$

where Q is written for a Cartesian system, V is the cell volume, nx and ny are components of the unity vector normal to the cell boundary, S is the flux area, E<sub>e</sub> and F<sub>e</sub> are the components of the convective, or Euler, flux vector, E<sub>v</sub> and F<sub>v</sub> are the components of the viscous, or diffusive, flux vector and G is the source term of the two-equation model. The vectors Q, E<sub>e</sub>, F<sub>e</sub>, E<sub>v</sub> and F<sub>v</sub> are, incorporating a k-ω formulation, represented by:

$$Q = \begin{pmatrix} \rho \\ \rho u \\ \rho v \\ e \\ \rho k \\ \rho s \end{pmatrix}, \quad E_e = \begin{pmatrix} \rho u \\ \rho u^2 + p \\ \rho uv \\ (e + p)u \\ \rho ku \\ \rho su \end{pmatrix}, \quad F_e = \begin{pmatrix} \rho v \\ \rho uv \\ \rho v^2 + p \\ (e + p)v \\ \rho kv \\ \rho sv \end{pmatrix};$$

$$E_v = \begin{pmatrix} 0 \\ t_{xx} + \tau_{xx} \\ t_{xy} + \tau_{xy} \\ f_x \\ \alpha_x \\ \beta_x \end{pmatrix}, \quad F_v = \begin{pmatrix} 0 \\ t_{xy} + \tau_{xy} \\ t_{yy} + \tau_{yy} \\ f_y \\ \alpha_y \\ \beta_y \end{pmatrix}, \quad G = \begin{pmatrix} 0 \\ 0 \\ 0 \\ 0 \\ G_k \\ G_s \end{pmatrix}, \quad (2)$$

where the components of the viscous stress tensor are defined as:

$$t_{xx} = [2\mu_M \partial u/\partial x - 2/3\mu_M (\partial u/\partial x + \partial v/\partial y)]/Re ; \\ t_{xy} = \mu_M (\partial u/\partial y + \partial v/\partial x)/Re ; \\ t_{yy} = [2\mu_M (\partial v/\partial y) - 2/3\mu_M (\partial u/\partial x + \partial v/\partial y)]/Re . \quad (3)$$

The components of the turbulent stress tensor (Reynolds stress tensor) are described by the following expressions:

$$\tau_{xx} = [2\mu_T \partial u/\partial x - 2/3\mu_T (\partial u/\partial x + \partial v/\partial y)]/Re - 2/3\rho k ; \\ \tau_{xy} = \mu_T (\partial u/\partial y + \partial v/\partial x)/Re ; \\ \tau_{yy} = [2\mu_T \partial v/\partial y - 2/3\mu_T (\partial u/\partial x + \partial v/\partial y)]/Re - 2/3\rho k . \quad (4)$$

Expressions to f<sub>x</sub> and f<sub>y</sub> are given bellow:

$$f_x = (t_{xx} + \tau_{xx})u + (t_{xy} + \tau_{xy})v - q_x ; \\ f_y = (t_{xy} + \tau_{xy})u + (t_{yy} + \tau_{yy})v - q_y, \quad (5)$$

where q<sub>x</sub> and q<sub>y</sub> are the Fourier heat flux components and are given by:

$$q_x = -\gamma/Re (\mu_M/Pr_L + \mu_T/Pr_T) \partial e_i/\partial x ; \\ q_y = -\gamma/Re (\mu_M/Pr_L + \mu_T/Pr_T) \partial e_i/\partial y . \quad (6)$$

The diffusion terms related to the k-ω equation are defined as:

$$\alpha_x = 1/Re (\mu_M + \mu_T^*/\sigma_k) \partial k/\partial x ; \\ \alpha_y = 1/Re (\mu_M + \mu_T^*/\sigma_k) \partial k/\partial y ; \\ \beta_x = 1/Re (\mu_M + \mu_T^*/\sigma_s) \partial s/\partial x ; \\ \beta_y = 1/Re (\mu_M + \mu_T^*/\sigma_s) \partial s/\partial y . \quad (7)$$

In the above equations, ρ is the fluid density; u and v are Cartesian components of the velocity vector in the x and y directions, respectively; e is the total energy per unit volume; p is the static pressure; k is the turbulence kinetic energy; s is the second turbulent variable, which can be the rate of dissipation of the turbulence kinetic energy (k-ε model) or the flow vorticity (k-ω model). In the present study, s = ω; the t's are viscous stress components; τ's are the Reynolds stress components; the q's are the Fourier heat flux components; G<sub>k</sub>

takes into account the production and the dissipation terms of  $k$ ;  $G_s$  takes into account the production and the dissipation terms of  $\omega$ ;  $\mu_M$  and  $\mu_T$  are the molecular and the turbulent viscosities, respectively;  $Pr_L$  and  $Pr_T$  are the laminar and the turbulent Prandtl numbers, respectively;  $\sigma_k$  and  $\sigma_s$  are turbulence coefficients;  $\gamma$  is the ratio of specific heats;  $Re$  is the laminar Reynolds number, defined by:

$$Re = \rho V_{REF} l_{REF} / \mu_M, \quad (9)$$

where  $V_{REF}$  is a reference flow velocity and  $l_{REF}$  is a configuration reference length. The internal energy of the fluid,  $e_i$ , is defined as:

$$e_i = e/\rho - 0.5(u^2 + v^2). \quad (10)$$

The Navier-Stokes equations are dimensionless in relation to the freestream density,  $\rho_\infty$ , the freestream speed of sound,  $a_\infty$ , and the freestream molecular viscosity,  $\mu_\infty$ . The system is closed by the state equation for a perfect gas:

$$p = (\gamma - 1) \left[ e - 0.5\rho(u^2 + v^2) - \rho k \right], \quad (11)$$

considering the ideal gas hypothesis. The total enthalpy is given by  $H = (e + p)/\rho$ .

#### A. Molecular Viscosity

The molecular viscosity model is based on the empiric Sutherland formula:

$$\mu_M = bT^{1/2} / (1 + S/T), \quad (12)$$

where  $T$  is the absolute temperature (K),  $b = 1.458 \times 10^{-6}$  Kg/(m.s.K<sup>1/2</sup>) and  $S = 110.4$  K, to the atmospheric air in the standard atmospheric conditions (see [44]).

### III. STEGER AND WARMING ALGORITHM

#### A. Theory for the one-dimensional case

If the homogeneous Euler equations are put in characteristic form

$$\partial W / \partial t + \Lambda \partial W / \partial x = 0, \quad (13)$$

where  $W$  is the vector of characteristic variables (defined in [45]) and  $\Lambda$  is the diagonal matrix of eigenvalues, the upwind scheme:

$$u_i^{n+1} - u_i^n = -\Delta t / \Delta x \left[ \hat{a}^+ (u_i^n - u_{i-1}^n) + \hat{a}^- (u_{i+1}^n - u_i^n) \right], \quad (14)$$

where  $u$  is a scalar property,  $\hat{a}^+ = 0.5(\hat{a} + |\hat{a}|)$  and  $\hat{a}^- = 0.5(\hat{a} - |\hat{a}|)$ , can be applied to each of the three

characteristic variables separately, with the definitions

$$\lambda_m^+ = 0.5(\lambda_m + |\lambda_m|) \quad \text{and} \quad \lambda_m^- = 0.5(\lambda_m - |\lambda_m|), \quad (15)$$

“m” assuming values from 1 to 4 (two-dimensional space), for each of the eigenvalues of  $\Lambda$

$$\Lambda = \begin{bmatrix} \lambda_1 & & \\ & \lambda_2 & \\ & & \lambda_3 \end{bmatrix} = \begin{bmatrix} u & & \\ & u+a & \\ & & u-a \end{bmatrix}. \quad (16)$$

This defines two diagonal matrices  $\Lambda^\pm$ :

$$\Lambda^\pm = \begin{bmatrix} \lambda_1^\pm & & \\ & \lambda_2^\pm & \\ & & \lambda_3^\pm \end{bmatrix} = \begin{bmatrix} \frac{(u \pm |u|)}{2} & & \\ & \frac{(u+a \pm |u+a|)}{2} & \\ & & \frac{(u-a \pm |u-a|)}{2} \end{bmatrix}, \quad (17)$$

where  $\Lambda^+$  has only positive eigenvalues,  $\Lambda^-$  only negative eigenvalues, and such that

$$\Lambda = \Lambda^+ + \Lambda^- \quad \text{and} \quad |\Lambda| = \Lambda^+ - \Lambda^-$$

or

$$\lambda_m = \lambda_m^+ + \lambda_m^- \quad \text{and} \quad |\lambda_m| = \lambda_m^+ - \lambda_m^-. \quad (18)$$

The quasi-linear coupled equations are obtained from the characteristic form by the transformation matrix  $P$  (defined in [45]), with the Jacobian  $A$  satisfying

$$A = PAP^{-1}, \quad \text{resulting in} \quad \partial Q / \partial t + A \partial Q / \partial x = 0. \quad (19)$$

Hence an upwind formulation can be obtained with the Jacobians

$$A^+ = PA^+P^{-1} \quad \text{and} \quad A^- = PA^-P^{-1}, \quad \text{with:}$$

$$A = A^+ + A^- \quad \text{and} \quad |A| = A^+ - A^-. \quad (20)$$

The fluxes associated with these split Jacobians are obtained from the remarkable property of homogeneity of the flux vector  $f(Q)$ .  $f(Q)$  is a homogeneous function of degree one of  $Q$ . Hence,  $f = AQ$  and the following flux splitting can be defined:

$$f^+ = A^+Q \quad \text{and} \quad f^- = A^-Q, \quad \text{with:} \quad f = f^+ + f^-. \quad (21)$$

This flux vector splitting, based on Eq. (15), has been introduced by [2]. The split fluxes  $f^+$  and  $f^-$  are also homogeneous functions of degree one in  $Q$ .

#### B. Arbitrary Meshes

In practical computations one deal mostly with arbitrary

meshes, considering either in a finite volume approach or in a curvilinear coordinate system.

In both cases, the upwind characterization is based on the signs of the eigenvalues of the matrix

$$K^{(n)} = \bar{A} \bullet \bar{n} = A n_x + B n_y. \tag{22}$$

The fluxes will be decomposed by their components

$$\tilde{F}^{(n)} = \tilde{F} \bullet \bar{n} = E n_x + F n_y \tag{23}$$

and separated into positive and negative parts according to the sign of the eigenvalues of  $K^{(n)}$  as described above, considering the normal direction as a local coordinate direction.

For a general eigenvalue splitting, as Eq. (15), the normal flux projection, Eq. (23), is decomposed by a [2] flux splitting as

$$\tilde{F}_{\pm}^{(n)} = \frac{\rho}{2\gamma} \left\{ \begin{array}{l} \alpha \\ \alpha u + a(\lambda_2^{\pm} - \lambda_3^{\pm}) n_x \\ \alpha v + a(\lambda_2^{\pm} - \lambda_3^{\pm}) n_y \\ \alpha \frac{u^2 + v^2}{2} + a v n (\lambda_2^{\pm} - \lambda_3^{\pm}) + a^2 \frac{\lambda_2^{\pm} + \lambda_3^{\pm}}{\gamma - 1} \end{array} \right\}, \tag{24}$$

where the eigenvalues of the matrix  $K$  are defined as

$$\lambda_1 = \bar{v} \bullet \bar{n} \equiv v_n, \lambda_2 = \bar{v} \bullet \bar{n} + a \text{ and } \lambda_3 = \bar{v} \bullet \bar{n} - a, \tag{25}$$

with  $\bar{v}$  is the flow velocity vector, and  $\pm$  sign indicates the positive or negative parts respectively. The parameter  $\alpha$  is defined as

$$\alpha = 2(\gamma - 1)\lambda_1^{\pm} + \lambda_2^{\pm} + \lambda_3^{\pm}. \tag{26}$$

*C. Numerical Scheme*

The numerical scheme of [2] implemented in this work is based on an unstructured finite volume formulation, where the convective numerical fluxes at interface are calculated as

$$\tilde{F}_1^{(m)} = \left[ \left( \tilde{F}_R^- \right)^{(m)} + \left( \tilde{F}_L^+ \right)^{(m)} \right] S^1, \tag{27}$$

where ‘‘R’’ and ‘‘L’’ represent right and left states, respectively,  $S$  is the cell face area and ‘‘1’’ indicates the flux interface. The subscript ‘‘L’’ is associated to properties of a given ‘‘i’’ cell and the subscript ‘‘R’’ is associated to properties of the ‘‘ne’’ neighbor cell of ‘‘i’’. The cell volume on an unstructured context is defined by:

$$V_i = 0.5 \left[ (x_{n1}y_{n2} + y_{n1}x_{n3} + x_{n2}y_{n3}) - (x_{n3}y_{n2} + y_{n3}x_{n1} + x_{n2}y_{n1}) \right], \tag{28}$$

with  $n1, n2$  and  $n3$  being the nodes of a given triangular cell,

defined in Fig. 1. Figure 1 exhibits the computational cell adopted for the simulations, as well its respective nodes, neighbors and flux interfaces.

The time integration is performed by an explicit method, second order accurate, Runge-Kutta type of five stages and can be represented of generalized form by:

$$\begin{aligned} Q_i^{(0)} &= Q_i^{(n)} \\ Q_i^{(k)} &= Q_i^{(0)} - \alpha_k \Delta t_i / V_i \times C(Q_i^{(k-1)}), \\ Q_i^{(n+1)} &= Q_i^{(k)} \end{aligned} \tag{29}$$

with  $k = 1, \dots, 5$ ;  $\alpha_1 = 1/4, \alpha_2 = 1/6, \alpha_3 = 3/8, \alpha_4 = 1/2$  and  $\alpha_5 = 1$ . The contribution of the convective numerical flux vectors is determined by the  $C_i$  vector:

$$C_i^{(m)} = \tilde{F}_1^{(m)} + \tilde{F}_2^{(m)} + \tilde{F}_3^{(m)}. \tag{30}$$

This version of the flux vector splitting algorithm of [2] is first order accurate in space.

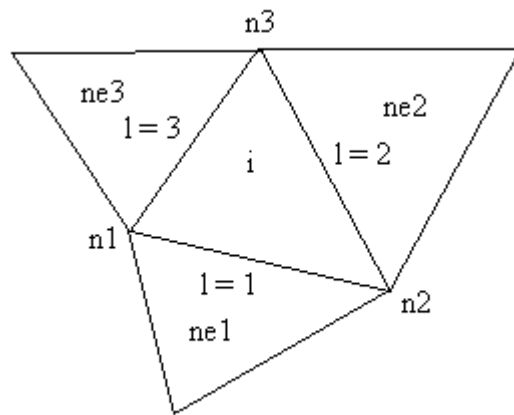


Figure 1. Schematic of a cell and its neighbors, nodes and flux interfaces.

IV. VAN LEER, LIOU AND STEFFEN JR., AND RADESPIEL AND KROLL ALGORITHMS

The space approximation of the integral Equation (1) to a triangular finite volume yields an ordinary differential equation system given by:

$$V_i dQ_i / dt = -C_i, \tag{31}$$

with  $C_i$  representing the net flux (residual) of the conservation of mass, conservation of momentum and conservation of energy in the volume  $V_i$ . The residual is calculated as:

$$C_i = F_1 + F_2 + F_3, \tag{32}$$

where  $F_1$  is the discrete convective minus diffusive flux at the interface ‘‘1’’.

The convective discrete flux calculated by the AUSM

scheme (Advection Upstream Splitting Method) can be interpreted as a sum involving the arithmetical average between the right (R) and the left (L) states of the “I” cell face, multiplied by the interface Mach number, and a scalar dissipative term. The subscript “L” is associated to properties of a given “i” cell and the subscript “R” is associated to properties of the “ne” neighbor cell of “i”. Hence, to the “I” interface:

$$F_1 = |S_1| \left[ \frac{1}{2} M_1 \left( \begin{bmatrix} \rho a \\ \rho a u \\ \rho a v \\ \rho a H \\ \rho a k \\ \rho a s \end{bmatrix}_i + \begin{bmatrix} \rho a \\ \rho a u \\ \rho a v \\ \rho a H \\ \rho a k \\ \rho a s \end{bmatrix}_{ne} \right) - \frac{1}{2} \phi_1 \begin{bmatrix} \rho a \\ \rho a u \\ \rho a v \\ \rho a H \\ \rho a k \\ \rho a s \end{bmatrix}_{ne} - \begin{bmatrix} \rho a \\ \rho a u \\ \rho a v \\ \rho a H \\ \rho a k \\ \rho a s \end{bmatrix}_i \right] + \begin{bmatrix} 0 \\ S_x p \\ S_y p \\ 0 \\ 0 \\ 0 \end{bmatrix}_1, \tag{33}$$

where  $S_1 = [S_x \ S_y]^T$  defines the normal area vector to the “I” surface. The area components at this interface are defined by:

$$S_x^1 = n_x^1 S^1 \quad \text{and} \quad S_y^1 = n_y^1 S^1. \tag{34}$$

The normal unity vector components,  $n_x^1$  and  $n_y^1$ , and the flux area of the “I” interface,  $S_1$ , are defined as:

$$n_x^1 = \Delta y_1 / (\Delta x_1^2 + \Delta y_1^2)^{0.5}, \quad n_y^1 = -\Delta x_1 / (\Delta x_1^2 + \Delta y_1^2)^{0.5} \\ \text{and} \quad S^1 = (\Delta x_1^2 + \Delta y_1^2)^{0.5}. \tag{35}$$

Expressions to  $\Delta x_1$  and  $\Delta y_1$  are given in Tab. 1. The quantity “a” represents the speed of sound, which is defined as:

$$a = (\gamma p / \rho - k)^{0.5}. \tag{36}$$

**Table 1 Values of  $\Delta x_1$  and  $\Delta y_1$ .**

Interface	$\Delta x_1$	$\Delta y_1$
1 = 1	$x_{n2} - x_{n1}$	$y_{n2} - y_{n1}$
1 = 2	$x_{n3} - x_{n2}$	$y_{n3} - y_{n2}$
1 = 3	$x_{n1} - x_{n3}$	$y_{n1} - y_{n3}$

$M_1$  defines the advection Mach number at the “I” face of the

“i” cell, which is calculated according to [4] as:

$$M_1 = M_L^+ + M_R^-, \tag{37}$$

where the separated Mach numbers  $M^{+/-}$  are defined by the [3] formulas:

$$M^+ = \begin{cases} M, & \text{if } M \geq 1; \\ 0.25(M+1)^2, & \text{if } |M| < 1; \\ 0, & \text{if } M \leq -1; \end{cases} \\ \text{and} \\ M^- = \begin{cases} 0, & \text{if } M \geq 1; \\ -0.25(M-1)^2, & \text{if } |M| < 1; \\ M, & \text{if } M \leq -1. \end{cases} \tag{38}$$

$M_L$  and  $M_R$  represent the Mach number associated with the left and right states, respectively. The advection Mach number is defined by:

$$M = (S_x u + S_y v) / (|S| a). \tag{39}$$

The pressure at the “I” face of the “i” cell is calculated by a similar way:

$$p_1 = p_L^+ + p_R^-, \tag{40}$$

with  $p^{+/-}$  denoting the pressure separation defined according to the [3] formulas:

$$p^+ = \begin{cases} p, & \text{if } M \geq 1; \\ 0.25p(M+1)^2(2-M), & \text{if } |M| < 1; \\ 0, & \text{if } M \leq -1; \end{cases} \\ \text{and} \\ p^- = \begin{cases} 0, & \text{if } M \geq 1; \\ 0.25p(M-1)^2(2+M), & \text{if } |M| < 1; \\ p, & \text{if } M \leq -1. \end{cases} \tag{41}$$

The definition of the dissipative term  $\phi$  determines the particular formulation of the convective fluxes. The following choice corresponds to the [3] algorithm, according to [6]:

$$\phi_1 = \phi_1^{VL} = \begin{cases} |M_1|, & \text{if } |M_1| \geq 1; \\ |M_1| + 0.5(M_R - 1)^2, & \text{if } 0 \leq M_1 < 1; \\ |M_1| + 0.5(M_L + 1)^2, & \text{if } -1 < M_1 \leq 0. \end{cases} \tag{42}$$

The above equations clearly show that to a supersonic cell face Mach number, the [3] scheme represents a discretization purely upwind, using either the left state or the right state to the convective terms and to the pressure, depending of the Mach number signal. This [3] scheme is first order accurate in space. The time integration is performed using an explicit Runge-Kutta method of five stages, second order accurate, and can be represented in generalized form by:

$$\begin{aligned} Q_i^{(0)} &= Q_i^{(n)} \\ Q_i^{(k)} &= Q_i^{(0)} - \alpha_k \Delta t_i \left[ C(Q_i^{(k-1)}) / V_{i,j} + G(Q_i^{(k-1)}) \right] \\ Q_i^{(n+1)} &= Q_i^{(k)} \end{aligned} \quad (43)$$

with  $k = 1, \dots, 5$ ;  $\alpha_1 = 1/4$ ,  $\alpha_2 = 1/6$ ,  $\alpha_3 = 3/8$ ,  $\alpha_4 = 1/2$  and  $\alpha_5 = 1$ ; and  $C = F_1 + F_2 + F_3$ . The  $G$  vector is used only in the turbulent simulations.

The [4] scheme is described by Eqs. (31) to (41) and (43). The next step is the determination of the  $\phi$  dissipative term. According to [6], the following choice for  $\phi$  results in the [4] scheme:

$$\phi_1^{LS} = |M_1| \quad (44)$$

Finally, the [6] algorithm is based on an hybrid scheme, which combines the [3] scheme, better resolution at shock regions, and the [4] (AUSM) scheme, better resolution at background regions. Hence,

$$\phi_1 = (1 - \omega)\phi_1^{VL} + \omega\phi_1^{LS}, \quad (45)$$

with:

$$\phi_1^{VL} = \begin{cases} |M_1|, & \text{if } |M_1| \geq 1; \\ |M_1| + \frac{1}{2}(M_R - 1)^2, & \text{if } 0 \leq M_1 < 1; \\ |M_1| + \frac{1}{2}(M_L + 1)^2, & \text{if } -1 < M_1 \leq 0; \end{cases}$$

and

$$\phi_1^{LS} = \begin{cases} |M_1|, & \text{if } |M_1| \geq \tilde{\delta} \\ \frac{(M_1)^2 + \tilde{\delta}^2}{2\tilde{\delta}}, & \text{if } |M_1| < \tilde{\delta} \end{cases}, \quad (46)$$

where  $\tilde{\delta}$  is a small parameter,  $0 < \tilde{\delta} \leq 0.5$ , and  $\omega$  is a constant,  $0 \leq \omega \leq 1$ . In this work, the values used to  $\tilde{\delta}$  and  $\omega$  were: 0.2 and 0.5, respectively. The time integration follows the method described by Eq. (43). This scheme is first order accurate in space.

The gradients of the primitive variables to the viscous flux are calculated using the Green theorem, which considers that the gradient of a primitive variable is constant at the volume

and that the volume integral which defines the gradient is replaced by a surface integral (see [37]). To the  $\partial u / \partial x$  gradient, for example, it is possible to write:

$$\begin{aligned} \frac{\partial u}{\partial x} &= \frac{1}{V} \int_V \frac{\partial u}{\partial x} dV = \frac{1}{V} \int_S u(\vec{n}_x \cdot d\vec{S}) = \frac{1}{V} \int_{S_x} u dS_x \cong \\ &= \frac{1}{V} [0.5(u_i + u_{ne1})S_{x_{i=1}} + 0.5(u_i + u_{ne2})S_{x_{i=2}} + 0.5(u_i + u_{ne3})S_{x_{i=3}}]. \end{aligned} \quad (47)$$

### V. RUMSEY, GATSKI, YING, AND BERTELTRUD TURBULENCE MODEL

In this work, the  $k-\omega$  model of [43] is the studied model, where  $s = \omega$ . The equilibrium eddy-viscosity term employed in the diffusion terms is given by

$$\mu_T^* = Re c_\mu^* \rho k / \omega, \quad (48)$$

where  $c_\mu^* = 0.081$ .

The explicit nonlinear constitutive equation that is used to close the Reynolds-averaged Navier-Stokes equations is given (after regularization)

$$\begin{aligned} \rho \tau_{ij} &= \frac{2}{3} \rho k \delta_{ij} - 2\mu_t \left( S_{ij} - \frac{1}{3} S_{kk} \delta_{ij} \right) - \frac{2\mu_t \alpha_3}{\omega} \left( S_{ik} W_{kj} + \right. \\ & \left. S_{jk} W_{ki} \right) + \frac{4\mu_t \alpha_2}{\omega} \left( S_{ik} S_{kj} - \frac{1}{3} S_{kl} S_{kl} \delta_{ij} \right), \end{aligned} \quad (49)$$

where

$$S_{ij} = \frac{1}{2} \left( \frac{\partial u_i}{\partial x_j} + \frac{\partial u_j}{\partial x_i} \right) \quad \text{and} \quad W_{ij} = \frac{1}{2} \left( \frac{\partial u_i}{\partial x_j} - \frac{\partial u_j}{\partial x_i} \right) \quad (50)$$

are the mean-rate-of-strain tensor and the mean-vorticity tensor, respectively. The turbulent viscosity  $\mu_T$  is

$$\mu_T = Re c_\mu \rho k / \omega. \quad (51)$$

and

$$c_\mu = \frac{3(1 + \eta^2) + 0.2(\eta^6 + \zeta^6)}{3 + \eta^2 + 6\eta^2 \zeta^2 + 6\zeta^2 + \eta^6 + \zeta^6} \alpha_1; \quad (52)$$

$$\eta = (\alpha_2 / \omega) (S_{ij} S_{ij})^{\frac{1}{2}} \quad \text{and} \quad \zeta = (\alpha_3 / \omega) (W_{ij} W_{ij})^{\frac{1}{2}}, \quad (53)$$

where  $\alpha_1 = (4/3 - C_2)(g/2)$ ,  $\alpha_2 = (2 - C_3)(g/2)$ ,  $\alpha_3 = (2 - C_4)(g/2)$  and  $g = (C_1/2 + C_5 - 1) - 1$ . The constants that govern the pressure-strain correlation model of [46] are  $C_1 = 6.8$ ,  $C_2 = 0.36$ ,  $C_3 = 1.25$ ,  $C_4 = 0.4$  and  $C_5 = 1.88$ . The  $\mu_T$  terms are given by

$$\mu_T = \text{Re } c_\mu \rho k / \omega, \tag{54}$$

where

$$c_\mu = \frac{3(1 + \eta^2)}{3 + \eta^2 + 6\eta^2\zeta^2 + 6\zeta^2 + \eta^6 + \zeta^6} \alpha_1. \tag{55}$$

The source term denoted by  $G$  in the governing equation contains the production and dissipation terms of  $k$  and  $\omega$ . To the [43] model, the  $G_k$  and  $G_\omega$  terms have the following expressions:

$$G_k = -P_k + D_k \quad \text{and} \quad G_\omega = -P_\omega + D_\omega, \tag{56}$$

where:

$$P_k = \rho \mu_T \left( \frac{\partial u}{\partial y} + \frac{\partial v}{\partial x} \right) \frac{\partial u}{\partial y}, \quad D_k = \rho \omega k / \text{Re};$$

$$P_\omega = \psi \rho \omega / k P_k, \quad \text{and} \quad D_\omega = \beta \rho \omega^2 / \text{Re}. \tag{57}$$

The closure coefficients adopted to the [43] model assume the following values:  $\beta = 0.83$ ;  $\kappa = 0.41$ ;  $\sigma_k = 1.4$ ;  $\sigma_\omega = 2.2$ ;  $\text{Prd}_L = 0.72$ ;  $\text{Prd}_T = 0.9$ ;  $\psi = \beta - \left[ \kappa^2 / \sigma_\omega \sqrt{c_\mu^*} \right]$ .

### VI. UNSTRUCTURED TRIANGULATION

An unstructured discretization of the calculation domain is usually recommended to complex configurations, due to the easily and efficiency that such domains can be discretized ([30], [47-49]). However, the unstructured mesh generation question will not be studied in this work. The unstructured meshes generated in this work were structured created and posteriorly the connectivity, neighboring, node coordinates and ghost tables were built in a pre-processing stage.

A study involving two types of domain triangulation is performed. In the first case, the mesh is generated with the triangles created in the same sense (see Fig. 2). In the second case, the triangles generated in one row is in a specific sense and in the above row is in an opposite sense (see Fig. 3), originating a mesh with more regular geometrical properties. It is important to emphasize that in the second method, the number of lines should be odd. These triangulation options are studied in the turbulent cases. As in [34-35] the alternated generation process should provide excellent results in symmetrical configurations. It is expected to be repeated in this study.

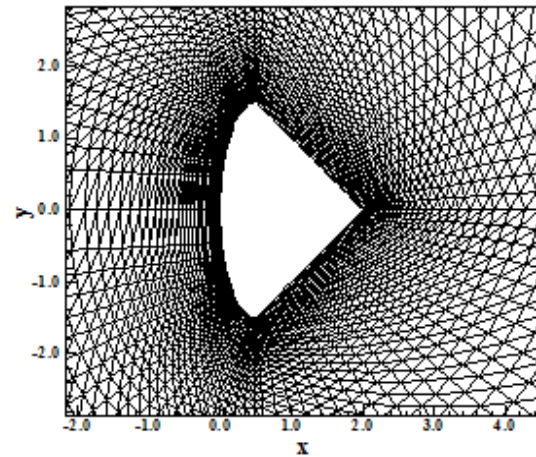


Figure 2. Triangulation in the Same Sense (SS).

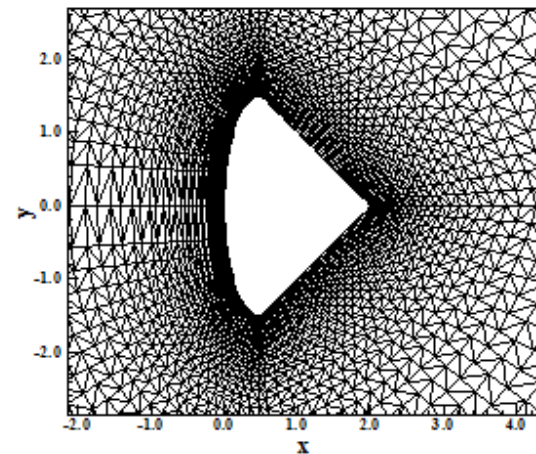


Figure 3. Triangulation in Alternate Sense (AS).

### VII. TIME STEP

As in [34-35, 38-39] the spatially variable time step procedure resulted in an excellent tool to accelerate convergence, it is repeated in this study with the expectation of also improve the convergence rate of the numerical schemes.

#### A. Spatially Variable Time Steps

The basic idea of the spatially variable time step procedure consists in keeping constant the CFL number in all calculation domain, allowing, hence, the use of appropriated time steps to each specific mesh region during the convergence process. In this work, two options of spatially variable time step, calculated in each iteration, were studied and are described below:

**Convective time step.** According to the definition of the CFL number, it is possible to write:

$$\Delta t_i = \text{CFL}(\Delta s)_i / c_i, \tag{58}$$

where: CFL is the ‘‘Courant-Friedrichs-Lewy’’ number to

provide numerical stability to the scheme;  $c_i = \left[ \left( u^2 + v^2 \right)^{0.5} + a \right]_i$  is the maximum characteristic velocity of information propagation in the calculation domain; and  $(\Delta s)_i$  is a characteristic length of information transport. Considering a finite volume context,  $(\Delta s)_i$  is chosen as the minor value found between the minor centroid distance, involving the “i” cell and a neighbor, and the minor cell side length.

**Convective + diffusive time step.** To a viscous simulation and according to the work of [49], it is possible to write:

$$\Delta t_i = \left( \frac{\text{CFL}(\Delta t_c \Delta t_v)}{\Delta t_c + \Delta t_v} \right)_i, \quad (59)$$

with  $\Delta t_c$  being the convective time step and  $\Delta t_v$  being the viscous time step. These quantities are defined as:

$$(\Delta t_c)_i = \frac{V_i}{(\lambda_c)_i}, \quad (\lambda_c)_i = \max(\lambda_{l=1}^{\max}, \lambda_{l=2}^{\max}, \lambda_{l=3}^{\max}); \quad (60)$$

$$\lambda_{\text{int}}^{\max} = \left( |u_{\text{int}} n_x + v_{\text{int}} n_y| + a_{\text{int}} \right) S_{\text{int}}; \quad (61)$$

$$(\Delta t_v)_i = K_v \frac{V_i}{(\lambda_v)_i}, \quad (p1)_i = \frac{\gamma^{3/2} M_\infty}{(\text{Re Pr } d_L)_i}; \quad (62)$$

$$(p2)_i = \frac{\mu_{l=1}}{\rho_{l=1}} S_{l=1}^2 + \frac{\mu_{l=2}}{\rho_{l=2}} S_{l=2}^2 + \frac{\mu_{l=3}}{\rho_{l=3}} S_{l=3}^2; \quad (63)$$

$$(\lambda_v)_i = (p1 \times p2)_i, \quad (64)$$

where interface properties are calculated by arithmetical average,  $M_\infty$  is the freestream Mach number,  $\mu$  is the fluid molecular viscosity and  $K_v$  is equal to 0.25, as recommended by [49].

## VIII. INITIAL AND BOUNDARY CONDITIONS

### A. Initial Condition

Freestream values, at all grid cells, are adopted for all flow properties as initial condition, as suggested by [30, 50]. Therefore, the vector of conserved variables is defined as:

$$Q_i = \left\{ 1 \quad M_\infty \cos \alpha \quad M_\infty \sin \alpha \quad \left[ \frac{1}{\gamma(\gamma-1)} + 0.5M_\infty^2 \right] \quad k_\infty \quad \omega_\infty \right\}^T, \quad (65)$$

where  $k_\infty$  is the freestream turbulent kinetic energy and  $\omega_\infty$  is the freestream turbulent vorticity. These parameters assumes the following values in the present work:  $k_\infty = 1.0 \times 10^{-6}$  and  $\omega_\infty = (10u_\infty / l_{\text{REF}})^2$ , with  $u_\infty$  being the freestream u Cartesian component of velocity and  $l_{\text{REF}}$  being a characteristic length,

the same adopted in the definition of the Reynolds number.

### B. Boundary Conditions

The boundary conditions are basically of five types: solid wall, entrance, exit, far field and continuity. These conditions are implemented with the help of ghost cells.

**Wall Condition.** Considering the inviscid case, this condition imposes the flow tangency at the solid wall. It is satisfied considering the wall tangent velocity component of the ghost volume as equals to the respective velocity component of its real neighbor cell. At the same way, the wall normal velocity component of the ghost cell is equaled in value, but with opposite signal, to the respective velocity component of the real neighbor cell. On the other hand, in the viscous case, it imposes the non-permeability and non-slip wall conditions. Therefore, the tangent velocity component of the ghost volume at wall has the same magnitude as the respective velocity component of its real neighbor cell, but opposite signal. In the same way, the normal velocity component of the ghost volume at wall is equal in value, but opposite in signal, to the respective velocity component of its real neighbor cell. These procedures lead to the following expressions to ughost and vghost, in each case:

$$\left. \begin{aligned} u_{\text{ghost}} &= (n_y^2 - n_x^2) u_{\text{real}} - (2n_x n_y) v_{\text{real}} \\ v_{\text{ghost}} &= -(2n_x n_y) u_{\text{real}} + (n_x^2 - n_y^2) v_{\text{real}} \end{aligned} \right\}, \quad (66)$$

to the inviscid case;

$$\left. \begin{aligned} u_{\text{ghost}} &= -u_{\text{real}} \\ v_{\text{ghost}} &= -v_{\text{real}} \end{aligned} \right\}, \quad (67)$$

to the viscous case.

The pressure gradient normal to the wall is assumed to be equal to zero, following an inviscid formulation or a boundary-layer like condition. The same hypothesis is applied to the temperature gradient normal to the wall, considering adiabatic wall. The ghost volume density and pressure are extrapolated from the respective values of the real neighbor volume (zero order extrapolation), with these two conditions. The total energy is obtained by the state equation of a perfect gas.

To the k- $\omega$  model, the turbulent kinetic energy and the turbulent vorticity at the wall ghost volumes are determined by the following expressions:

$$k_{\text{ghost}} = 0.0 \quad \text{and} \quad \omega_{\text{ghost}} = \left[ (38/3 v_M) / (\beta d_n^2) \right]^2, \quad (68)$$

where  $\beta$  assumes the value 3/40 and  $d_n$  is the distance of the first centroid point to the wall.

**Entrance Condition.** The entrance condition considers subsonic and supersonic flow. They are detailed below:

(a) Subsonic flow: Five properties are specified and one extrapolated. This approach is based on information propagation analysis along characteristic directions in the calculation domain (see [50]). In other words, for subsonic flow, five characteristic propagate information point into the computational domain. Thus five flow properties must be fixed at the inlet plane. Just one characteristic line allows information to travel upstream. So, one flow variable must be extrapolated from the grid interior to the inlet boundary. The pressure was the extrapolated variable from the real neighbor volumes, for all studied problems. Density and velocity components adopted values of freestream flow. To the  $k-\omega$  model, the turbulence kinetic energy and the turbulence vorticity assume the values of the initial condition (freestream flow). The total energy is determined by the state equation of a perfect gas.

(b) Supersonic flow: In this case no information travels upstream; therefore all variables are fixed with their freestream values.

**Exit Condition.** Again, two flow situations are analyzed. They are detailed below:

(a) Subsonic flow: Five characteristic propagate information outward the computational domain. Hence, the associated variables should be extrapolated from interior information. The characteristic direction associated to the “(qnormal-a)” velocity should be specified because it point inward to the computational domain (see [50]). In this case, the ghost volume pressure is specified from its initial value. Density, velocity components, the turbulence kinetic energy and the turbulence vorticity are extrapolated. The total energy is obtained from the state equation of a perfect gas.

(b) Supersonic flow: All variables are extrapolated from interior grid cells, as no flow information can make its way upstream. In other words, nothing can be fixed.

**Far field Condition.** This condition is only needed to the turbulent variables, once the far field is also an entrance and/or exit boundary. The mean flow kinetic energy is assumed to be  $K = 0.5u^2$  and the turbulence kinetic energy at the far field adopts the value  $k_{ff} = 0.01K$ , or 1% of  $K$ . The turbulence vorticity is determined by its freestream value.

**Continuity Condition.** This condition requires the flow continuity at the trailing edge of the re-entry capsule (Kutta condition). It is done considering the vector of conserved variables at the trailing edge lower-surface as equal to the vector of conserved variables at the trailing edge upper-surface.

## IX. RESULTS

Simulations were performed using a personal notebook with processor INTEL core i7 and 8GBytes of RAM memory. The convergence criterion consisted of a reduction of four (4)

orders in the magnitude of the residual. The residual was defined as the maximum value of the discretized equations. As one have four (4) equations to the inviscid case and six (6) equations to the turbulent case, each one should be tested to obtain the value of the maximum discretized equation for each cell. Comparing all discretized equation values, one obtains the maximum residual in the field. The entrance or attack angle in the present simulations was adopted equal to  $0.0^\circ$ . The value of  $\gamma$  was estimated in 1.4 for “cold gas” flow simulations. Two problems were studied: the air inlet (inviscid case) and the re-entry capsule (turbulent case).

### A. Inviscid Solutions

In the inviscid case, it was studied the hypersonic flow along an air inlet configuration. The freestream Mach number was adopted equal to 10.0, a “cold gas” hypersonic flow. The air inlet configuration and mesh are show in Figs. 4 and 5, respectively. To this problem only the same sense mesh orientation (SS) was studied. This mesh is composed of 6,000 triangular cells and 3,111 nodes, which corresponds to a mesh of  $61 \times 51$  points in a finite difference context.

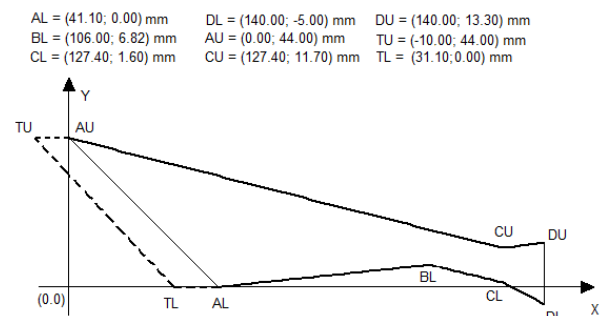


Figure 4. Air inlet configuration.

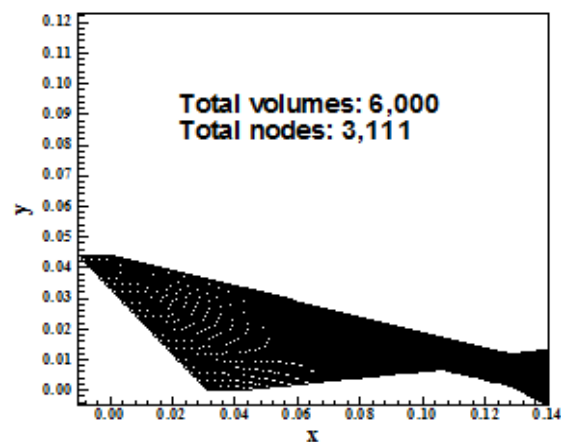


Figure 5. Air inlet mesh.

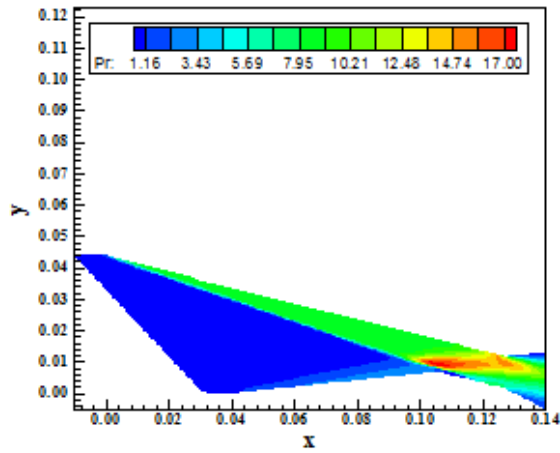


Figure 6. Pressure contours ([2]).

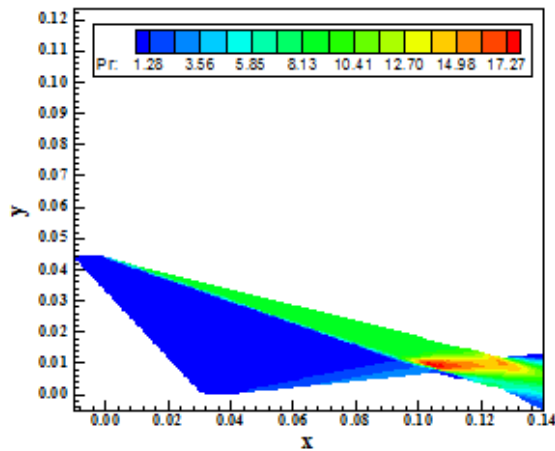


Figure 7. Pressure contours ([3]).

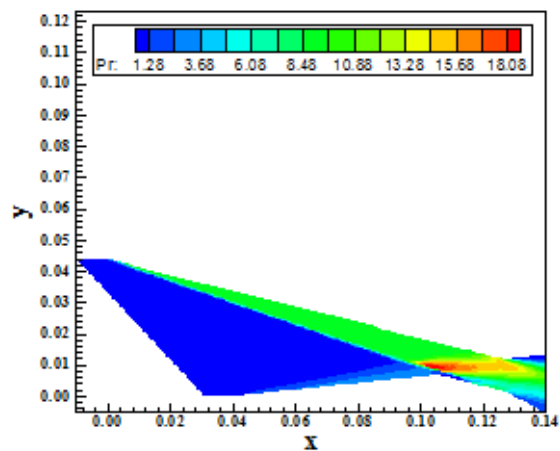


Figure 8. Pressure contours ([4]).

Figures 6 to 9 exhibit the pressure contours obtained by [2-4, 6] schemes to a first order solution. All schemes capture appropriately the shock waves at the upper and lower surfaces of the air inlet. The shock interference at the inlet throat is well

captured. Oscillations are not present, which indicates that the wall pressure distributions of each scheme are smooth and well defined. The most severe pressure field is obtained by the [4] scheme, identifying such algorithm as more conservative than the others for this case.

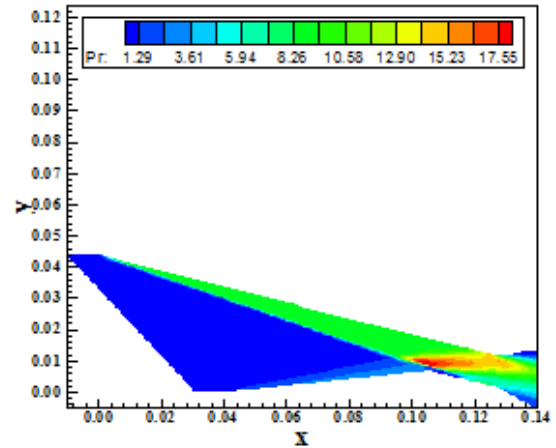


Figure 9. Pressure contours ([6]).

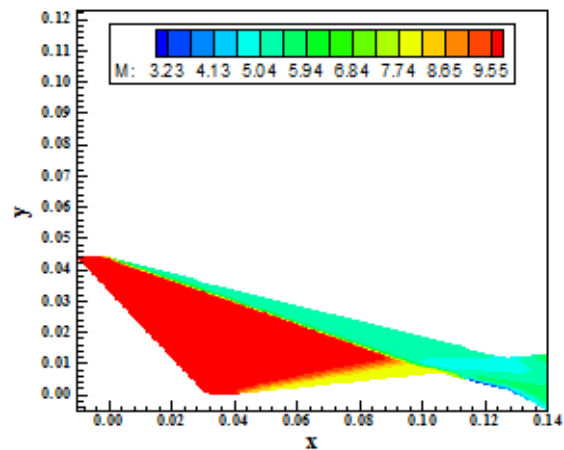


Figure 10. Mach number contours ([2]).

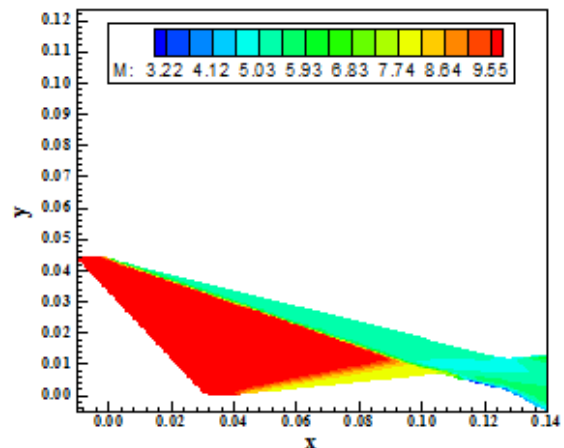


Figure 11. Mach number contours ([3]).

Figures 10 to 13 present the Mach number contours obtained by all four algorithms [2-4, 6]. The solutions are of good quality, without oscillations. The shock waves are well captured by the schemes. The most intense Mach number field is found in the [2-3] solutions.

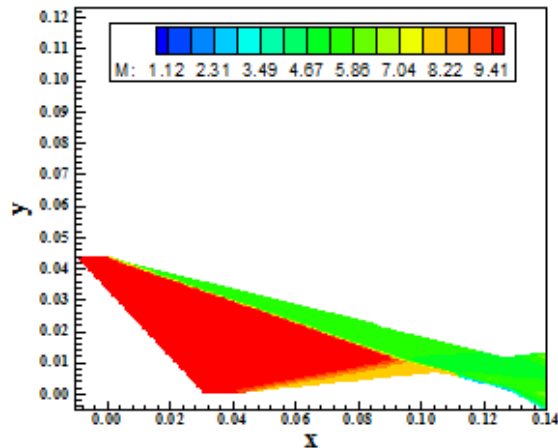


Figure 12. Mach number contours ([4]).

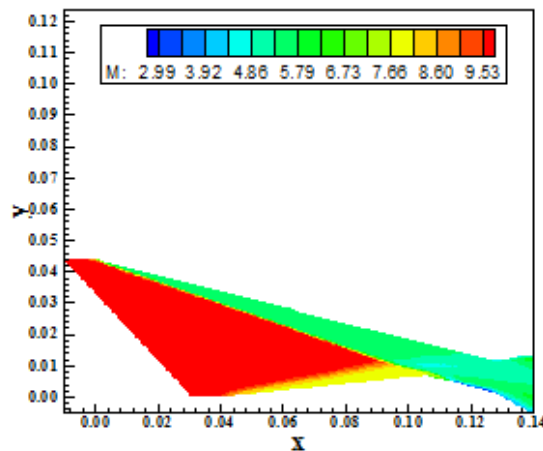


Figure 13. Mach number contours ([6]).

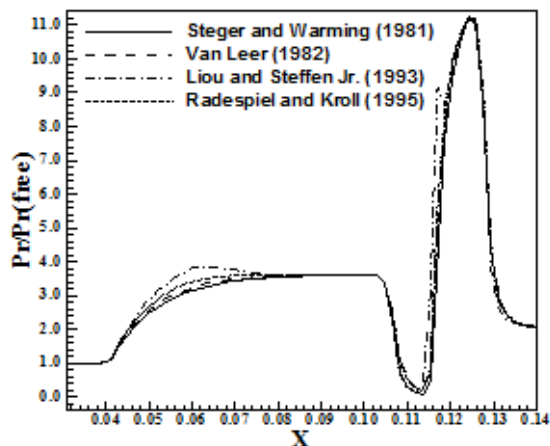


Figure 14. Pressure distributions.

Figure 14 presents the wall pressure distribution at the air inlet lower wall. All solutions converge to approximately the same curve. The shock interference is well characterized by the depression in the pressure curve at about 0.114 m. The smooth behavior of the pressure distribution at the air inlet entrance characterizes this region as a compression wave and not as an oblique shock wave, whence discontinuities in the flow properties would be distinguishable.

One way to quantitatively verify if the solutions generated by each scheme are satisfactory consists in determining the shock angle of the oblique shock waves at the lower and upper air inlet walls, measured in relation to the initial direction of the flow field. [51] (pages 352 and 353) presents a diagram with values of the shock angle,  $\beta$ , to oblique shock waves. The value of this angle is determined as function of the freestream Mach number and of the deflection angle of the flow after the shock wave,  $\phi$ . With a transfer were measured the inclination angles of the lower and upper ramp's walls of the entrance device. To the lower wall this angle was of  $\phi_L = 6.5^\circ$  in relation to the horizontal and to the upper wall was of  $\phi_U = 13.5^\circ$  in relation to the horizontal. With these angles and with the freestream Mach number was possible to determine the theoretical shock angles of the oblique shock waves. These angles are disposed in Tab. 2, joined with the measured values of them to each numerical scheme and the respective percentage error. Using again a transfer in Figures 6 to 9, it is possible to obtain the values of  $\beta$  to each scheme, as well the respective errors, shown in Tab. 2. The results highlight the [3] scheme as the most accurate of the studied versions, with error of 10.0%, to the lower wall, and 4.6%, to the upper wall.

Table 2 Measured values of the shock angles of the oblique shock waves.

Surface	Scheme	$\beta$ (Theory)	$\beta$ (Measured)	Error (%)
Lower	[2]	10.0	11.0	10.0
	[3]	10.0	11.0	10.0
	[4]	10.0	12.0	20.0
	[6]	10.0	11.3	13.0
Upper	[2]	17.5	20.0	14.3
	[3]	17.5	18.3	4.6
	[4]	17.5	19.6	12.0
	[6]	17.5	20.1	14.9

#### B. Turbulent Solutions – Same Sense Mesh Generation

In this work, only the  $k-\omega$  model of [43] is analyzed. Initially the SS case was considered.

The re-entry capsule configuration is shown in Fig. 15, whereas the re-entry capsule mesh, generated in the SS case, is exhibited in Fig. 16. The freestream Mach number of 9.0 was studied, which corresponds to the maximum value of this parameter that each algorithm was able to support. Only the [3, 6] algorithms were tested in this example. Only first order solutions were obtained. The Reynolds number is estimated in  $2.14 \times 10^6$  and in the viscous case an exponential stretching of 7.5% was employed in the  $\eta$  direction.

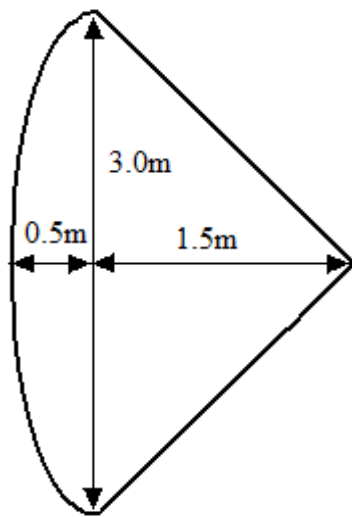


Figure 15. Re-entry capsule configuration.

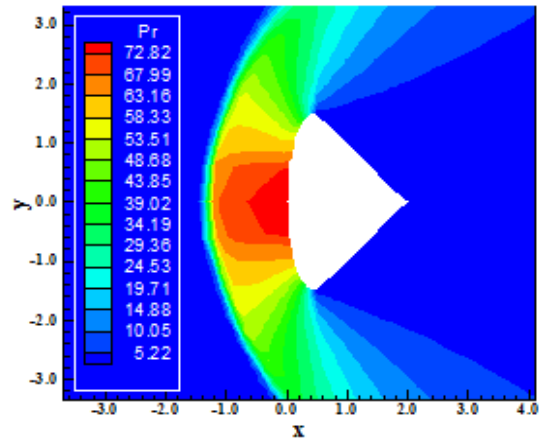


Figure 18. Pressure contours ([6]).

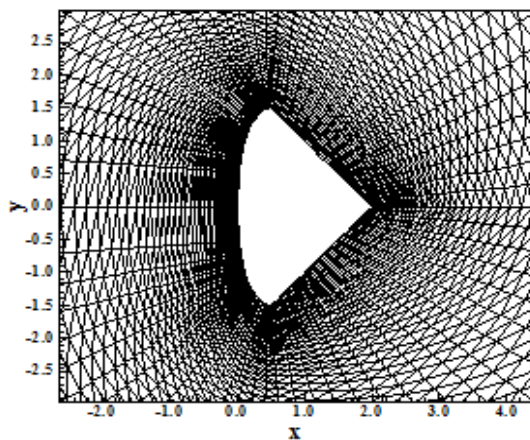


Figure 16. Re-entry capsule mesh (SS case).

Figures 17 and 18 exhibit the pressure contours obtained by the [3, 6] numerical algorithms, respectively. Both pressure fields are identically in quantitative terms, although in qualitative terms some discrepancies are observed close to the blunt surface of the re-entry configuration.

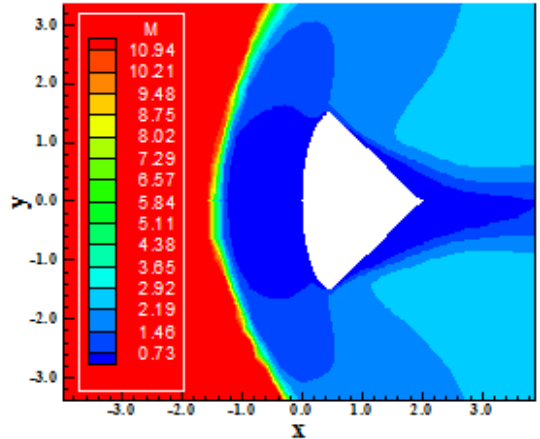


Figure 19. Mach number contours ([3]).

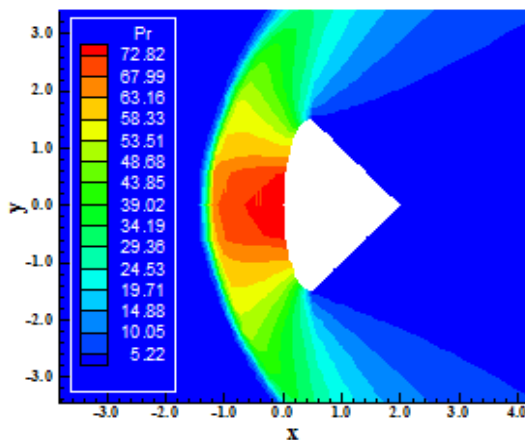


Figure 17. Pressure contours ([3]).

Figures 19 and 20 show the Mach number contours generated by the [3, 6] schemes, respectively. Both solutions are very close, with the formation of a wake at the trailing edge. Non-symmetry is noted at the wake, which is an indicative that the separation region behind the re-entry capsule geometry presents an unsymmetrical behavior. This consideration implies that the pair of circulation bubbles that is formed in this region is unsymmetrical too. The [3] contours are smoother than the [6] contours.

Figures 21 and 22 exhibit the velocity vector field and the streamlines around the re-entry capsule configuration. The [6] solution presents a small non-symmetry characteristic at the trailing edge. Both solutions present a wake formed at the trailing edge and this wake is not positioned at the body's symmetry line, indicating a non-symmetry zone. Afterwards it will be shown that it is characteristic of the mesh generation process and that the AS generation process eliminates this solution aspect. In general, the solutions are good. It is possible to identify the formation of a pair of circulation bubbles at the trailing edge, in both solutions, resulting from wake viscous effect. As can be noted, the pair of circulation

bubble presents no symmetry in relation to the capsule symmetry line, which originates a non-physical result. As was observed in the early studies ([34-35, 38-39]), the AS mesh orientation overcome this characteristic of the SS mesh orientation.

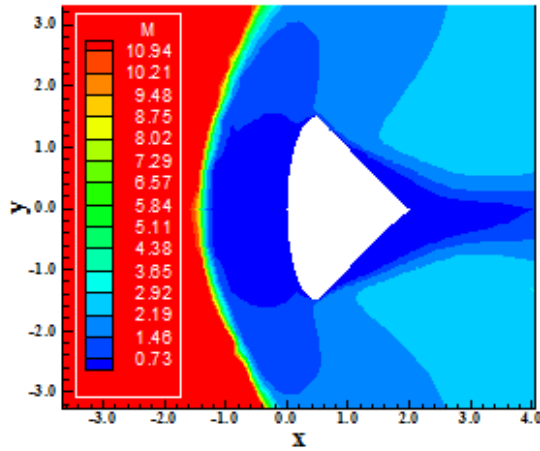


Figure 20. Mach number contours ([6]).

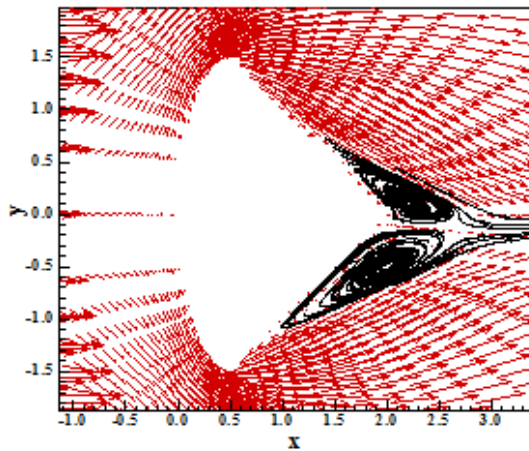


Figure 21. Velocity field and streamlines ([3]).

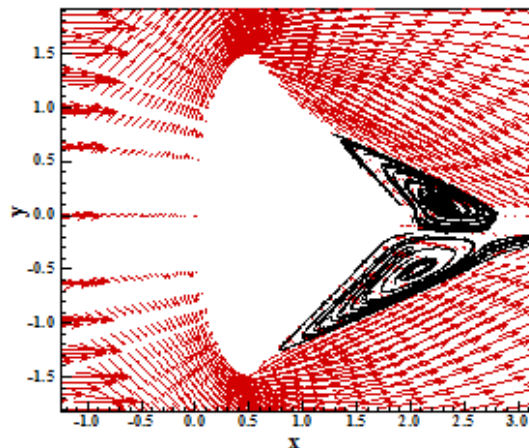


Figure 22. Velocity field and streamlines ([6]).

Figure 23 shows the wall pressure distributions obtained by the [3, 6] schemes, in terms of  $-C_p$  distribution. The solutions are very close, without meaningful differences. The  $-C_p$  plateau equal to zero indicates that at the separation region the pressure is constant and has its freestream value. In other words, in a region of great exchange of energy, the pressure is constant and equal to its freestream value. The  $C_p$  peak at the re-entry capsule leading edge is approximately 1.92 for both schemes. The variation of  $-C_p$  at the ellipse region is practically linear, without great variations.

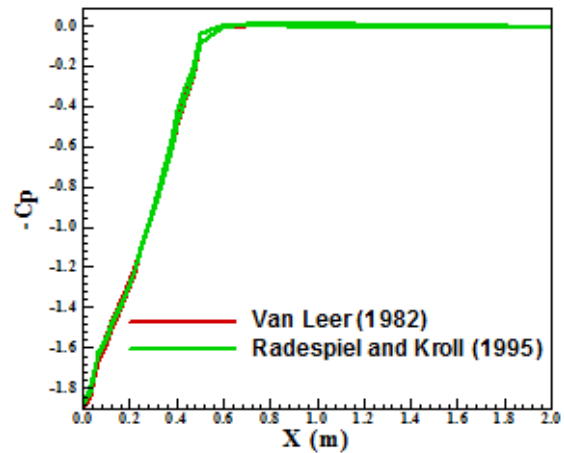


Figure 23.  $-C_p$  distributions at wall.

Figure 24 exhibits the turbulent kinetic energy profile obtained at the node 58, by the [3, 6] algorithms. As can be seen, the  $k$  distributions are very close with some differences in the boundary layer region. Moreover, the kinetic energy of the [6] scheme is bigger than the respective energy of the [3] scheme. It means that the [6] scheme remove more kinetic energy of the mean flow than the [3] scheme does.

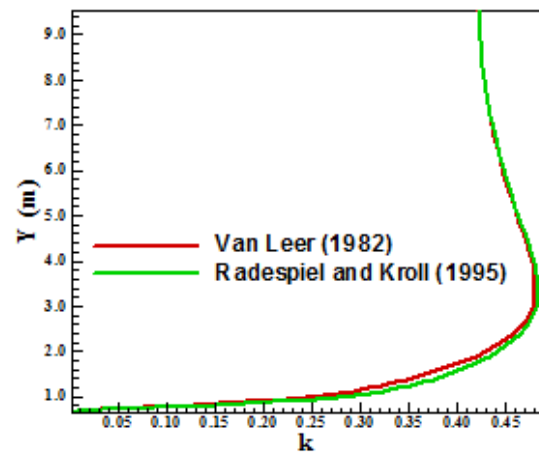


Figure 24. Turbulent kinetic energy.

Figure 25 shows the turbulent vorticity profile obtained at the node 58, by the [3, 6] numerical schemes. As can be noted, the vorticity is more intense close to the wall, into the

boundary layer region, where it is formed. The intensity of the vorticity is of the order of 107 unities, indicating strong vorticity interaction in this region. Note that the vorticity is a maximum close to the wall.

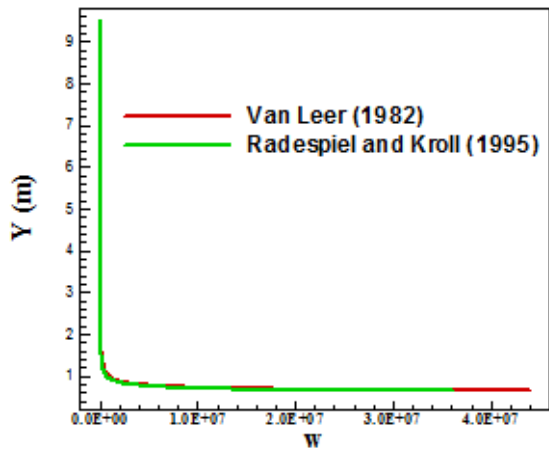


Figure 25. Turbulent vorticity.

Figure 26 presents the u velocity profile, calculated at node 58, obtained by both numerical schemes. Both solutions agree in qualitative and quantitative terms and both reaches the boundary layer edge at the same Y position. The u profile presents a reverse flow close to  $y = 0.0$  and characterizes as turbulent profile because of the large width close to the wall and a linear behavior approaching the boundary edge.

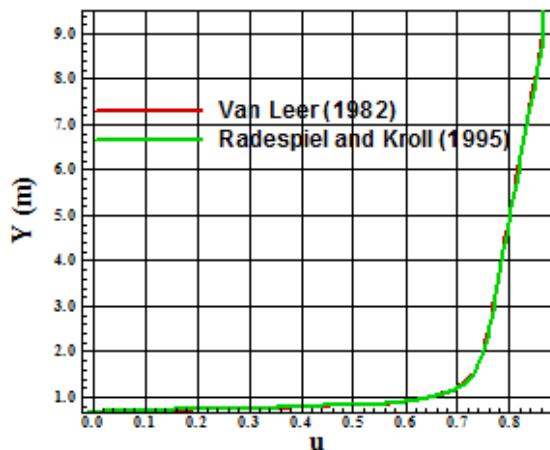


Figure 26. u profile.

*C. Turbulent Solutions – Alternated Sense Mesh Generation*

A detail of the employed mesh in the present study generated by the AS process is shown below, in Fig. 27.

Figures 28 and 29 exhibit the pressure contours obtained by [3, 6] numerical algorithms, in the re-entry capsule problem, as [43] is employed. The most severe pressure field is obtained by the [3] scheme, characterizing this one as more conservative for this AS case.

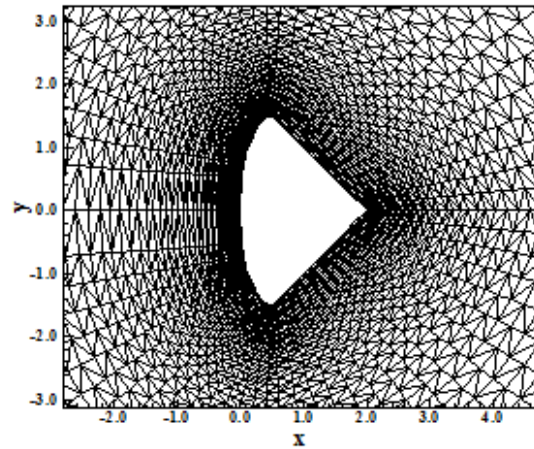


Figure 27. Re-entry capsule mesh (AS case).

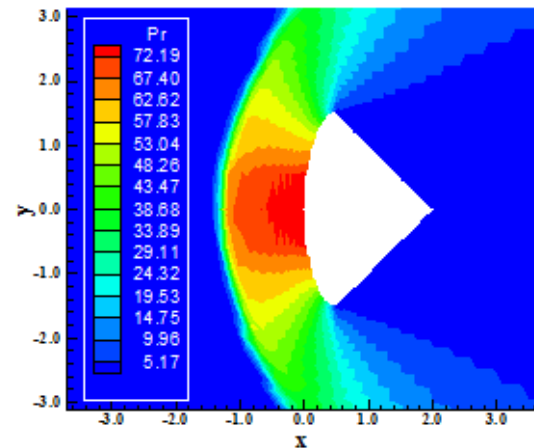


Figure 28. Pressure contours ([3]).

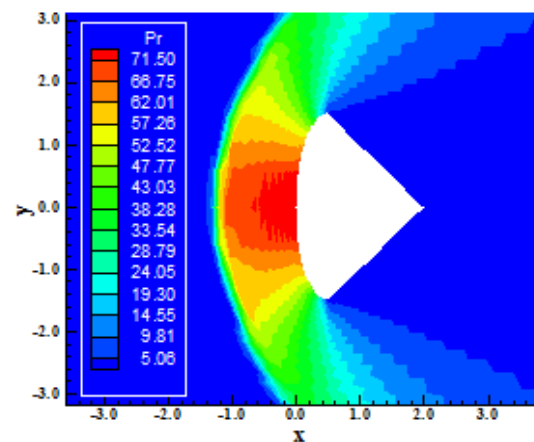


Figure 29. Pressure contours ([6]).

Figures 30 and 31 show the Mach number fields obtained by the [3, 6] algorithms, respectively. Both Mach number field are similar in quantitative terms, presenting some small differences in qualitative aspects. Figures 32 and 33 exhibit the velocity field and the streamlines generated by both schemes in

the AS case. The circulation bubbles formed at the boundary layer region due to flow detachment present better symmetry properties than in the SS case. Again, such mesh orientation generation process provides better characteristics to the numerical schemes, allowing a more appropriated capture of non-linear flow aspects.

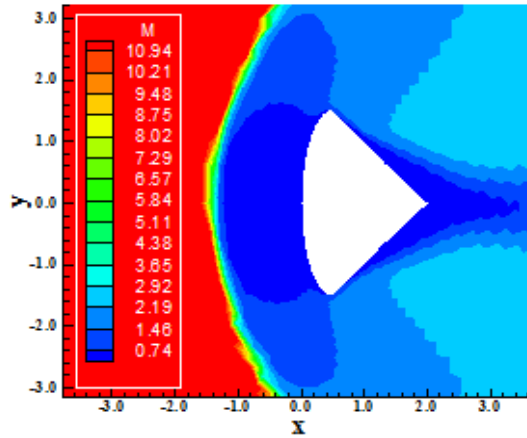


Figure 30. Mach number contours ([3]).

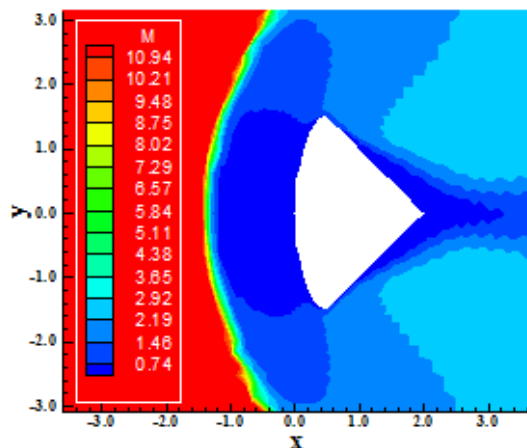


Figure 31. Mach number contours ([6]).

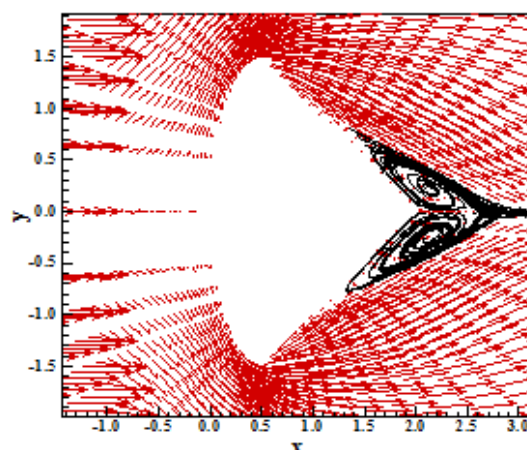


Figure 32. Velocity field ad streamlines ([3]).

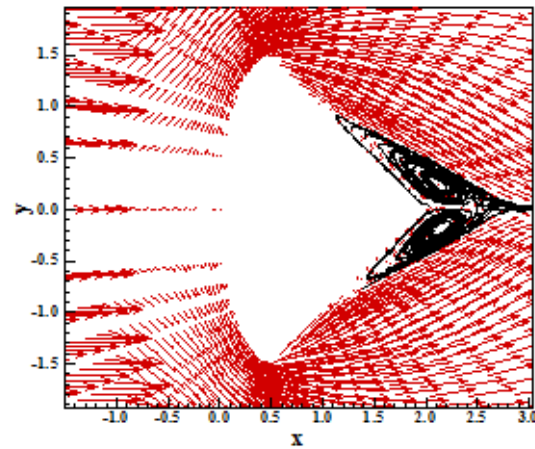


Figure 33. Velocity field and streamlines ([6]).

Figures 32 and 33 present the velocity field and the streamlines obtained by the numerical algorithms of [3, 6], employing the [43] turbulence model. The vortices distribution is symmetric in relation to the body's symmetry axis. The wake is aligned with the body's symmetry axis. The adherence and impermeability conditions required by the Navier-Stokes equations are plenty satisfied. The boundary layer separation and the shock wave are well captured by the numerical algorithms, which ratifies these ones as efficient numerical tools to be used in absence of a high resolution scheme. They are upwind schemes with good capturing properties of the flow discontinuity.

Figure 34 exhibits the  $-C_p$  distributions at wall obtained by the [3, 6] algorithms as using the [43] turbulence model. The peak of  $C_p$  is equal to 1.92, the same obtained in the SS simulations. The  $C_p$  plateau is also captured, as occurred in the SS case. Both solutions – [3, 6] – present similar behavior, not being possible identify one better than the other.

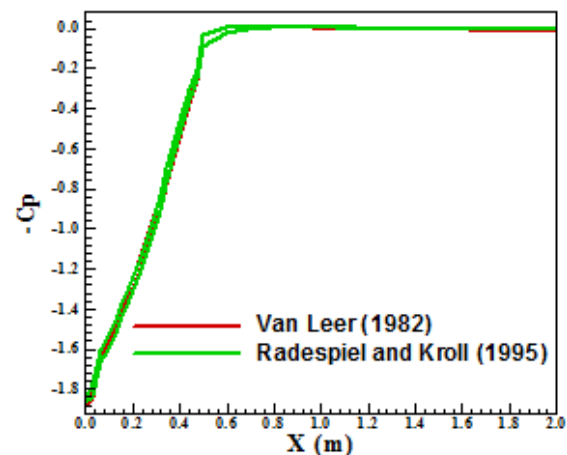


Figure 34.  $-C_p$  distributions at wall.

Figure 35 presents the turbulent kinetic energy profile generated by the numerical schemes under study. There are

small differences between the solutions. The [6] scheme characterizing the flow a little more turbulent than the [3] scheme does. In quantitative terms, the difference is small.

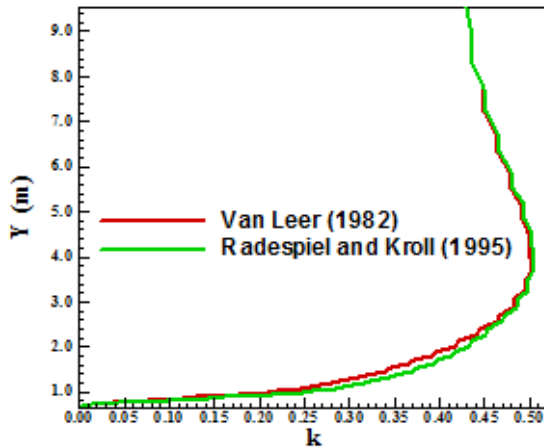


Figure 35. Turbulent kinetic energy.

Figure 36 shows the turbulent vorticity profile obtained by the [3, 6] algorithms employing the [43] turbulence model. The biggest value of vorticity is found close to the wall and assumes a dimensionless value of  $5 \times 10^7$ . Far from the wall the vorticity is zero because there are no vortices at the far field. The local of great exchange of energy, due to the cascade of energy, is close to the wall, where the vortices are created and propagated, interacting among themselves.

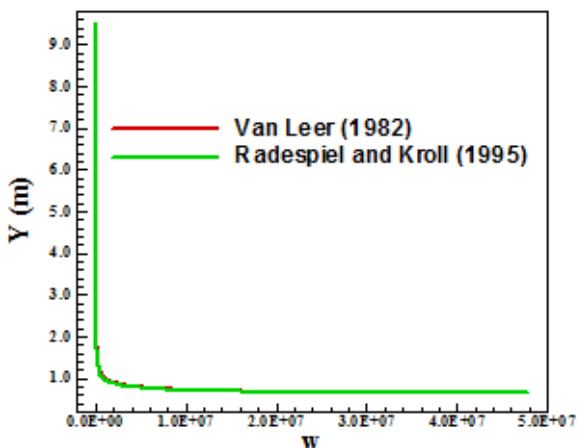


Figure 36. Turbulent vorticity.

Figure 37 exhibits the  $u$  profile. This dimensionless profile is typical of a turbulent flow, indicating that the present study is valid. A reverse flow region is identified by both algorithms close to the wall. The cut off behavior observed in some profiles is due to the mesh generation process. Note that in the SS case, the cut off effect is not present. It is due to the continuity in the ordination of the cells and neighbors. In the AS case this ordination is more spread out. The good solution aspects observed in this work, in the inviscid and turbulent

flows, justifies such use and ratifies the affirmation done in [35].

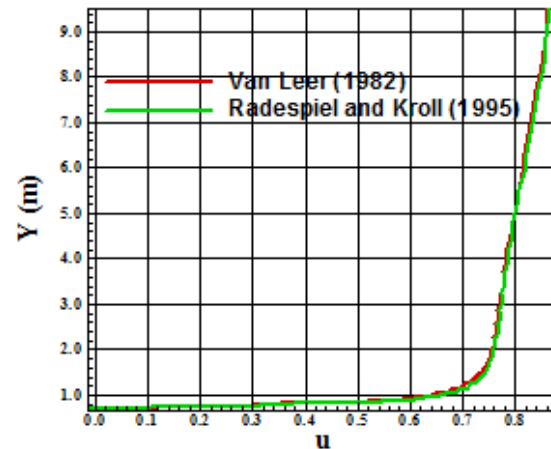


Figure 37.  $u$  profile.

#### D. Stagnation Pressure Estimation

One possibility to quantitative comparison of both schemes and the [43] turbulence model is the determination of the stagnation pressure ahead of the configuration. [51] presents a table of normal shock wave properties in its B Appendix. This table permits the determination of some shock wave properties as function of the freestream Mach number. In front of the re-entry capsule configuration, the shock wave presents a normal shock behaviour, which permits the determination of the stagnation pressure, behind the shock wave, from the tables encountered in [51]. It is possible to determine the ratio  $pr_0/pr_\infty$  from [51], where  $pr_0$  is the stagnation pressure in front of the configuration and  $pr_\infty$  is the freestream pressure (equals to  $1/\gamma$  with the present dimensionless). Hence, to the present case one has  $pr_0/pr_\infty = 104.80$ , resulting in  $pr_0 = 74.83$ .

Table 3 shows the values of the stagnation pressure obtained by the [3, 6] to the [43] turbulence model studied in this work for the case  $M_\infty = 9.0$ . Errors less than 4.50% were found, which is not better than the results obtained in [39], for the same problem and the same Mach number case.

Table 3 Values of stagnation pressure.

Scheme	Orientation	$pr_0$	Error (%)
[3]	SS	72.82	2.69
[3]	AS	72.19	3.53
[6]	SS	72.82	2.69
[6]	AS	71.50	4.45

#### E. Inviscid Conclusions

In quantitative terms the [3] scheme present the best value to the upper and lower shock angles of the air inlet configuration, characterizing such algorithm as providing accurate results to hypersonic flow problems, even in its first-order accuracy. As

final conclusion, the [3] algorithm is more recommended to perform inviscid simulations: it was better than the others algorithms in the studies before and in the present study.

#### F. Turbulent Viscous Conclusions

As conclusion of the turbulent viscous calculations it is possible to affirm that the [3] scheme is more conservative than the [6] scheme. The former is also more accurate in the determination of the stagnation pressure at the configuration nose. It is also possible to conclude that the [40] turbulence model, analyzed in [38-39], is the most robust among the tested models. The [41], in its four variants, presented limited robustness properties, but it is also as accurate as the [40] model is. The [42] turbulence model is an intermediate one: better than the [41] in terms of robustness and worse than the [40] in terms of accuracy. The [43] turbulence model has presented good performance, capturing the main aspects of the fluid flow, like: boundary layer detachment, vortices formation, pressure plateau, etc. The [43] turbulence model, although not so robust than the [40] model, presents the same characteristics of the other four turbulence models tested along this work. At the end of this journey, it is possible to highlight that the [40] model, with errors below 4.10% in the estimation of the stagnation pressure ahead of the re-entry capsule configuration, is the best one studied in this work. The AS mesh generation process was again the most appropriate choose to yield meshes of good quality, in terms of symmetry and in the determination of the shock wave thickness. The reducing in the shock wave thickness and the good distribution of the vortices in relation to the body's symmetry line are highlighted aspects of this process and guarantees or ratifies such choose when treating unstructured spatial discretization.

#### X. CONCLUSIONS

In this work, fifth of this study, numerical simulations involving supersonic and hypersonic flows on an unstructured context are analysed. The [3, 6] schemes are implemented on a finite volume formulation, using unstructured spatial discretization. The algorithms are implemented in their first order spatial accuracy. The hypersonic air inlet problem was studied considering the inviscid formulation. It aims to identify the main aspects of the [2-4, 6] algorithms in the capture of the shock interference and high "cold gas" non-linear features of such flow regime. To the turbulent simulations, the [43] model is employed to solve the re-entry capsule problem. The results have demonstrated that the [3] algorithm yields the best results in terms of the prediction of the shock angles of the oblique shock waves in the air inlet problem and the best value of the stagnation pressure at the configuration nose in the re-entry capsule configuration. The spatially variable time step is the best choice to accelerate the convergence of the numerical schemes, as reported by [21-22]. This paper is the conclusion of Maciel's works started in 2011 and treats mainly the influence of the turbulence model on the solution quality.

#### ACKNOWLEDGMENT

The author acknowledges the infra-structure of the ITA that allowed the realization of this work.

#### REFERENCES

- [1] P. Kutler, "Computation of Three-Dimensional, Inviscid Supersonic Flows", Lecture Notes in Physics, Vol. 41, 1975, pp. 287-374.
- [2] J. L. Steger, and R. F. Warming, "Flux Vector Splitting of the Inviscid Gasdynamic Equations with Application to Finite-Difference Methods", Journal of Computational Physics, Vol. 40, 1981, pp. 263-293.
- [3] B. Van Leer, "Flux-Vector Splitting for the Euler Equations", Proceedings of the 8th International Conference on Numerical Methods in Fluid Dynamics, E. Krause, Editor, Lecture Notes in Physics, Vol. 170, 1982, pp. 507-512, Springer-Verlag, Berlin.
- [4] M. Liou, and C. J. Steffen Jr., "A New Flux Splitting Scheme", Journal of Computational Physics, Vol. 107, 1993, pp. 23-39.
- [5] P. L. Roe, "Approximate Riemann Solvers, Parameter Vectors, and Difference Schemes", Journal of Computational Physics, Vol. 43, 1981, pp. 357-372.
- [6] R. Radespiel, and N. Kroll, "Accurate Flux Vector Splitting for Shocks and Shear Layers", Journal of Computational Physics, Vol. 121, 1995, pp. 66-78.
- [7] E. Turkel, and B. Van Leer, "Flux-Vector Splitting and Runge-Kutta Methods for the Euler Equations", ICASE Report 84-27; also NASA CR 172415, 1984.
- [8] D. W. Riggins, R. W. Walters, and D. Pelletier, "The use of Direct Solvers for Compressible Flow Computations", AIAA Paper 88-0229, 1988.
- [9] D. Mavriplis, and A. Jameson, "Multigrid Solution of the Euler Equations on Unstructured and Adaptive Meshes", ICASE Report 87-53; also NASA CR 178346, 1987.
- [10] T. J. Barth, and D. C. Jespersen, "The Design and Application of Upwind Schemes on Unstructured Meshes", AIAA Paper 89-0336, 1989.
- [11] B. Stoufflet, J. Périaux, F. Fezoui, and A. Dervieux, "Numerical Simulation of 3-D Hypersonic Euler Flows Around Space Vehicles Using Adapted Finite-Elements", AIAA Paper 87-0560, 1987.
- [12] D. L. Whitaker, "Two-Dimensional Euler Computations on a Triangular Mesh Using an Upwind, Finite-Volume Scheme", Ph.D. Thesis, Dept. of Aerospace and Ocean Engineering, Virginia Polytechnic Inst. and State Univ., Blacksburg, VA, 1988.
- [13] E. S. G., Maciel, "Comparison Between the First Order Upwind Unstructured Algorithms of Roe and of Harten in the Solution of the Euler Equations in Two-Dimensions", Proceedings of the XIX Congress of Mechanical Engineering (XIX COBEM), Brasília, DF, Brazil, 2007.
- [14] E. S. G., Maciel, "Comparison Between the First Order Upwind Unstructured Algorithms of Steger and Warming and of Van Leer in the Solution of the Euler Equations in Two-Dimensions", Proceedings of the XIX Congress of Mechanical Engineering (XIX COBEM), Brasília, DF, Brazil, 2007.
- [15] A. Harten, "High Resolution Schemes for Hyperbolic Conservation Laws", Journal of Computational Physics, Vol. 49, 1983, pp. 357-393.
- [16] Maciel, E. S. G., "Comparison Among the Unstructured Algorithms of Frink, Parikh and Pirzadeh, of Liou and Steffen, and of Radespiel and Kroll in the Solution of the Euler Equations in 2D - Theory", Proceedings of the 8th Symposium of Computational Mechanics (VIII SIMMEC), Belo Horizonte, MG, Brazil, 2008.
- [17] E. S. G., Maciel, "Comparison Among the Unstructured Algorithms of Frink, Parikh and Pirzadeh, of Liou and Steffen, and of Radespiel and Kroll in the Solution of the Euler Equations in 2D - Results", Proceedings of the 8th Symposium of Computational Mechanics (VIII SIMMEC), Belo Horizonte, MG, Brazil, 2008.
- [18] N. T. Frink, P. Parikh, and S. Pirzadeh, "Aerodynamic Analysis of Complex Configurations Using Unstructured Grids", AIAA 91-3292-CP, 1991.
- [19] E. S. G. Maciel, "Extension of the Unstructured Algorithms of Liou and Steffen Jr. and of Radespiel and Kroll to Second Order Accuracy Employing Linear Reconstruction and Application to the Euler Equations in 2D - Theory", Proceedings of the XX International Congress of Mechanical Engineering (XX COBEM), Gramado, RS, Brazil, 2009.
- [20] E. S. G. Maciel, "Extension of the Unstructured Algorithms of Liou and Steffen Jr. and of Radespiel and Kroll to Second Order Accuracy Employing Linear Reconstruction and Application to the Euler Equations in 2D - Results", Proceedings of the XX International

- Congress of Mechanical Engineering (XX COBEM), Gramado, RS, Brazil, 2009.
- [21] E. S. G. Maciel, "Analysis of Convergence Acceleration Techniques Used in Unstructured Algorithms in the Solution of Aeronautical Problems – Part I", Proceedings of the XVIII International Congress of Mechanical Engineering (XVIII COBEM), Ouro Preto, MG, Brazil, 2005.
- [22] E. S. G. Maciel, "Analysis of Convergence Acceleration Techniques Used in Unstructured Algorithms in the Solution of Aerospace Problems – Part II", Proceedings of the XII Brazilian Congress of Thermal Engineering and Sciences (XII ENCIT), Belo Horizonte, MG, Brazil, 2008.
- [23] E. S. G. Maciel, "Extensão dos Algoritmos Não Estruturados de Roe e de Van Leer para Segunda Ordem de Precisão Usando Reconstrução Linear e Aplicação às Equações de Euler em 2D – Teoria", Anales del II Congreso Argentino de Ingeniería Mecánica (II CAIM), San Juan, Argentina, 2010.
- [24] E. S. G. Maciel, "Extensão dos Algoritmos Não Estruturados de Roe e de Van Leer para Segunda Ordem de Precisão Usando Reconstrução Linear e Aplicação às Equações de Euler em 2D – Resultados", Anales del II Congreso Argentino de Ingeniería Mecánica (II CAIM), San Juan, Argentina, 2010.
- [25] E. S. G. Maciel, "Estudo de Escoamentos Turbulentos Utilizando os Modelos de Cebeci e Smith e de Baldwin e Lomax e Comparação entre os Algoritmos de MacCormack e de Jameson e Mavriplis", Proceedings of the VII Symposium of Computational Mechanics (VII SIMMEC), Araxá, MG, Brazil, 2006.
- [26] E. S. G. Maciel, "Comparação entre os Modelos de Turbulência de Cebeci e Smith e de Baldwin e Lomax", Proceedings of the V Spring School of Transition and Turbulence (V EPTT), Rio de Janeiro, RJ, Brazil, 2006.
- [27] T. Cebeci, and A. M. O. Smith, "A Finite-Difference Method for Calculating Compressible Laminar and Turbulent Boundary Layers", Journal of Basic Engineering, Trans. ASME, Series B, Vol. 92, No. 3, 1970, pp. 523-535.
- [28] B. S. Baldwin, and H. Lomax, "Thin Layer Approximation and Algebraic Model for Separated Turbulent Flows", AIAA Paper 78-257, 1978.
- [29] R. W. MacCormack, "The Effect of Viscosity in Hypervelocity Impact Cratering", AIAA Paper 69-354, 1969.
- [30] A. Jameson, and D. Mavriplis, "Finite Volume Solution of the Two-Dimensional Euler Equations on a Regular Triangular Mesh", AIAA Journal, Vol. 24, No. 4, 1986, pp. 611-618.
- [31] E. S. G. Maciel, "Comparison Between the Two-Equation Turbulence Models of Jones and Launder and of Wilcox and Rubesin Applied to an Aeronautical Problem", Proceedings of the 12th Pan-American Congress of Applied Mechanics (PACAM XII), Port of Spain, Trinidad, 2012.
- [32] W. P. Jones, and B. E. Launder, "The Prediction of Laminarization with a Two-Equation Model of Turbulence", International Journal of Heat and Mass Transfer, Vol. 15, 1972, pp. 301-304.
- [33] D. C. Wilcox, and M. W. Rubesin, "Progress in Turbulence Modeling for Complex Flow Fields Including the Effects of Compressibility", NASA TP-1517, 1980.
- [34] E. S. G. Maciel, "Supersonic and Hypersonic Flows on 2D Unstructured Context: Part I", WSEAS Transactions on Fluid Dynamics, Vol. 6, October, Issue 4, 2011, pp. 199-226.
- [35] E. S. G. Maciel, "Supersonic and Hypersonic Flows on 2D Unstructured Context: Part II", WSEAS Transactions on Fluid Dynamics, Vol. 6, October, Issue 4, 2011, pp. 227-256.
- [36] F. Jacon, and D. Knight, "A Navier-Stokes Algorithm for Turbulent Flows Using an Unstructured Grid and Flux Difference Splitting", AIAA Paper 94-2292, 1994.
- [37] L. N. Long, M. M. S. Khan, and H. T. Sharp, "Massively Parallel Three-Dimensional Euler / Navier-Stokes Method", AIAA Journal, Vol. 29, No. 5, 1991, pp. 657-666.
- [38] E. S. G. Maciel, "Supersonic and Hypersonic Flows on 2D Unstructured Context: Part III Other Turbulence Models", WSEAS Transactions on Applied and Theoretical Mechanics (under review).
- [39] E. S. G. Maciel, "Supersonic and Hypersonic Flows on 2D Unstructured Context: Part IV Other Turbulence Models", WSEAS Transactions on Applied and Theoretical Mechanics, Vol. 8, April, Issue 2, 2013, pp. 109-135.
- [40] D. C. Wilcox, "Reassessment of the Scale-Determining Equation for Advanced Turbulence Models", AIAA Journal, Vol. 26, No. 11, 1988, pp. 1299-1310.
- [41] F. R. Menter, and C. L. Rumsey, "Assessment of Two-Equation Turbulence Models for Transonic Flows", AIAA Paper 94-2343, 1994.
- [42] D. A. Yoder, N. J. Georgiadids, and P. D. Orkwis, "Implementation of a Two-Equation k-omega turbulence model in NPARC", AIAA Paper 96-0383, 1996.
- [43] C. L. Rumsey, T. B. Gatski, S. X. Ying, and A. Bertelrud, "Prediction of High-Lift Flows Using Turbulent Closure Models", AIAA Journal, Vol. 36, No. 5, 1998, pp. 765-774.
- [44] R. W. Fox, and A. T. McDonald, "Introdução à Mecânica dos Fluidos", Ed. Guanabara Koogan, Rio de Janeiro, RJ, Brazil, 632 p, 1988.
- [45] C. Hirsch, "Numerical Computation of Internal and External Flows – Computational Methods for Inviscid and Viscous Flows", John Wiley & Sons Ltd, 691 p, 1990.
- [46] C. G. Speziale, S. Sarkar, and T. B. Gatski, "Modeling the Pressure-Strain Correlation of Turbulence: An Invariant Dynamical Systems Approach", Journal of Fluid Mechanics, Vol. 227, 1991, pp. 245-272.
- [47] D. J. Mavriplis, "Accurate Multigrid Solution of the Euler Equations on Unstructured and Adaptive Meshes", AIAA Journal, Vol. 28, No. 2, 1990, pp. 213-221.
- [48] S. Pirzadeh, "Structured Background Grids for Generation of Unstructured Grids by Advancing Front Method", AIAA Paper 91-3233-CP, 1991.
- [49] D. J. Mavriplis, and A. Jameson, "Multigrid Solution of the Navier-Stokes Equations on Triangular Meshes", AIAA Journal, Vol. 28, No. 8, 1990, pp. 1415-1425.
- [50] E. S. G. Maciel, "Simulação Numérica de Escoamentos Supersônicos e Hipersônicos Utilizando Técnicas de Dinâmica dos Fluidos Computacional", Ph.D. Thesis, ITA, CTA, São José dos Campos, SP, Brazil, 2002.
- [51] J. D. Anderson Jr., "Fundamentals of Aerodynamics", McGraw-Hill, Inc., 563p, 1984.

**Edisson S. G. Maciel** (F'14), born in 1969, february, 25, in Recife, Pernambuco. He is a Mechanical Engineering undergraduated by UFPE in 1992, in Recife, PE, Brazil; Mester degree in Thermal Engineering by UFPE in 1995, in Recife, PE, Brazil; Doctor degree in Aeronautical Engineering by ITA in 2002, in São José dos Campos, SP, Brazil; and Post-Doctor degree in Aeronautical Engineering by ITA in 2009, in São José dos Campos, SP, Brazil.

Actually, he is working in a new post-doctorate project in Aerospace Engineering at ITA. The last researches are based on thermochemical non-equilibrium reentry simulations in Earth and thermochemical non-equilibrium entry simulations in Mars. They are: Maciel, E. S. G., and Pimenta, A. P., "Thermochemical Non-Equilibrium Reentry Flows in Two-Dimensions – Part I", WSEAS Transactions on Mathematics, Vol. 11, Issue 6, June, pp. 520-545, 2012; Maciel, E. S. G., and Pimenta, A. P., "Thermochemical Non-Equilibrium Entry Flows in Mars in Two-Dimensions – Part I", WSEAS Transactions on Applied and Theoretical Mechanics, Vol. 8, Issue 1, January, pp. 26-54, 2013; and he has three published books, the first one being: Maciel, E. S. G., "Aplicações de Algoritmos Predictor-Corretor e TVD na Solução das Equações de Euler e de Navier-Stokes em Duas Dimensões", Recife, PE, Editor UFPE, 2013. He is interested in the Magnetogasdynamic field with applications to fluid dynamics and in the use of ENO algorithms.